Slip velocity boundary conditions for the lattice Boltzmann modeling of microchannel flows

Goncalo Silva, Irina Ginzburg

Received: 28 January 2022 | Revised: 30 March 2022 | Accepted: 7 August 2022

DOI: 10.1002/fld.5138

RESEARCH ARTICLE

WILEY

Slip velocity boundary conditions for the lattice Boltzmann modeling of microchannel flows

Goncalo Silva[1] | **Irina Ginzburg**[2]

[1]IDMEC, Mechatronics Department, University of Évora, Évora, Portugal

[2]Université Paris-Saclay, INRAE, UR HYCAR, Antony, France

Correspondence
Goncalo Silva, IDMEC, Mechatronics Department, University of Évora, R. Romão Ramalho 59, 7000-671 Évora, Portugal.
Email: gnsilva@uevora.pt

Irina Ginzburg, Université Paris-Saclay, INRAE, UR HYCAR, 92160 Antony, France.
Email: irina.ginzburg@inrae.fr

Funding information
FCT, Grant/Award Number: UIDB/50022/2020

Abstract

Slip flows in ducts are important in numerous engineering applications, most notably in microchannel flows. Compared to the standard no-slip Dirichlet condition, the case of slip formulates as a Robin-type condition for the fluid tangential velocity. Such an increase in mathematical complexity is accompanied by a more challenging numerical transcription. The present work concerns with this topic, addressing the modeling of the slip velocity boundary condition in the lattice Boltzmann method (LBM) applied to steady slow viscous flows inside ducts of nontrivial shapes. As novelty, we extend the newly revised local second-order boundary (LSOB) Dirichlet fluid flow method [*Philos. Trans. R. Soc. A* 378, 20190404 (2020)] to implement the slip velocity condition within the two-relaxation-time (TRT) framework. The LSOB follows an in-node philosophy where its operation principle seeks to explicitly reconstruct the unknown boundary populations in the form of a third-order accurate Chapman–Enskog expansion, where the wall slip condition is built-in as a normal Taylor-type condition. The key point of this approach is that the required first- and second-order momentum derivatives, rather than computed through nonlocal finite difference approximations, are locally determined through a simple local linear algebra procedure, whose formulation is particularly aided by the TRT symmetry argument. To express the obtained derivatives, two approaches are considered, called Lnode and Lwall, which operate with node and wall variables, respectively. These two formulations are developed to prescribe the physical slip condition over plane and curved walls, including the corners. Their consistency and accuracy characteristics are examined against alternative linkwise strategies to impose the wall slip velocity, such as the kinetic-based diffusive bounce-back scheme, the central linear interpolation slip scheme, and the multireflection slip scheme. The several slip schemes are tested over different 3D microchannel configurations, with walls not conforming with the LBM uniform mesh. Numerical tests confirm the advanced accuracy characteristics of the proposed LSOB slip boundary scheme, revealing the added challenge of the wall slip modeling, and that parabolic accuracy is a necessary requirement to reach second-order accuracy within this problem class.

KEYWORDS

lattice Boltzmann method, rarefied gases, slip boundary conditions, two-relaxation-time

1 | INTRODUCTION

The study of laminar viscous flows is important in many engineering fields.[1] While this problem is often considered under no-slip boundary conditions, numerous applications exist where a slip velocity boundary condition is necessary;[2,3] examples range from the flow over lubricated or coated surfaces[4] (e.g., Teflon), sedimentation processes in environmental engineering,[5,6] flows of emulsions, suspensions, foam or polymer solutions,[7] flows over rough surfaces,[8,9] superhydrophobic nanosurfaces,[10] and so forth. Another important field where the fluid wall slip plays the dominant role occurs in rarefied gas flows within microchannels,[11-18] which is the application case motivating the present study.

Taking an arbitrary solid wall surface defined by the unit inward normal vector $\vec{n}$ and the tangential vector $\vec{t}$, the slip velocity boundary condition[3,11,19,20] for a rarefied gas flowing parallel to the wall tangent direction is written as follows:

$$u_t(\vec{x}_w) - U_t|_{\text{wall}} = C\ \lambda\ \partial_n u_t(\vec{x}_w), \tag{1}$$

where C is a slippage coefficient $\mathcal{O}(1)$, supporting different values[3,12,21,22] based on the gas or the gas-surface conditions and λ is the gas mean-free-path, a microscopic length scale, which together with the macroscopic length scale, defined here based on the microchannel hydraulic diameter D_h, measures the degree of rarefaction of the gaseous flow. This ratio establishes the Knudsen (Kn) number, the main physical governing parameter in this problem class:

$$\text{Kn} = \frac{\lambda}{D_h}. \tag{2}$$

The present work is limited to physical regimes within $0.001 \leq \text{Kn} \leq 0.1$, that is, the so-called *slip flow regime*. Here, the effect of rarefaction is only manifested on the fluid-wall interactions. This way, conventional hydrodynamics equations remain valid in bulk and only the no-slip velocity condition gets replaced by a slip one, to account for the finite Kn phenomena. Outside this Kn interval, it is agreed[3,11,17] that for $\text{Kn} < 0.001$ the hydrodynamic regime, where the no-slip condition holds, is a viable one, whereas for $\text{Kn} > 0.1$ the effect of rarefaction is no longer restricted to a sole jump on the macroscopic fluid properties at the wall, but extends towards the bulk flow solution, creating the so-called Knudsen layers, a feature beyond the scope of this work. Slip flow theory has a rigorous theoretical foundation for gaseous flows, as established by Sone.[16] Yet, the application of Equation (1) has also a vast theoretical and empirical[7-10] support in liquid flows under the concept of slip length, with $\ell := C\ \lambda$ set in Equation (1). This makes the application of Equation (1) useful in both gas and liquid flows undergoing wall slip. In microchannel flows, the accurate modeling of the slip velocity condition gains even more relevance as with the scale reduction the effect of surface-based phenomena (where fluid-wall interactions fit in) tends to dominate over (bulk) volumetric ones.[3,13,17]

The numerical approximation of the slip boundary condition within computational fluid dynamics (CFD) models remains an active area of research.[3,14,15,17,23] Contrary to the no-slip condition, the slip velocity boundary condition, Equation (1), is a Robin-type condition for the velocity tangential component u_t, relating its value to the normal derivative at the boundary. Such a mixed structure may lead to compatibility problems between the numerical approximation of bulk and boundary derivatives.[14,24] Additionally, the wall impermeability condition $u_n = U_n|_{\text{wall}}$ applied over the normal velocity component u_n remains of the Dirichlet-type. Hence, any velocity slip numerical model will have to deal with the different mathematical nature of each velocity component in a consistent fashion, otherwise distortions may be created on the velocity profile accommodation at the boundary.[21,22,24-28]

To model complex fluid flow phenomena the lattice Boltzmann method (LBM)[29-32] has been recognized as a very competent, alternative CFD approach. In the context of slip flows, the development of LBM boundary models has been mostly exploited on the basis of the LBM kinetic heritage; namely, by searching over discrete analogs of the kinetic boundary conditions formulated at the level of the continuous Boltzmann equation.[33] Unfortunately, the slip boundary condition that results from these "kinetic-based" LBM schemes is often contaminated by unavoidable discrete lattice effects; a list of them has been pointed out in past studies.[21,22,34,35] It turns out that, in simple flows, where the LBM solution can be obtained analytically, these errors can be "absorbed" into physical terms so that an effective slip[21,34] can be recovered. However, in general flow configurations, this kind of numerical calibration is not doable, which is evident by the recovery of numerical solutions that do not converge to the intended physical solution as the mesh size goes to zero.[21,22]

In order to consistently approximate the wall slip condition, Equation (1), the structure of the closure relation that boundary conditions in LBM should satisfy over arbitrary shaped wall discretizations has been deduced as a Taylor-type

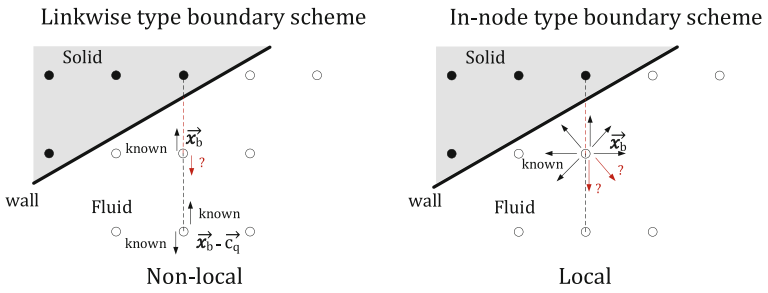

FIGURE 1 Schematic illustration of the operation principle guiding linkwise and in-node boundary schemes. The linkwise type schemes express the unknown incoming populations through a linear combination of the known components (often nonlocal), all restricted to the same link. The in-node type schemes determine the unknown incoming populations through a linear combination of the known components outcoming from the same node (local), but pertaining to different links. [Colour figure can be viewed at wileyonlinelibrary.com]

closure relation.[21,22] Moreover, it has been shown[21,22] how to satisfy this closure relation based on linkwise (directional) boundary schemes.[21,22] In this context, the general and theoretically transparent framework offered by multireflection (MR) rules[26-28] was adopted. As an outcome for LBM users, it was indicated how to incorporate the slip condition into the coefficients of the well-established MR schemes. To the best of the authors' knowledge, those MR slip schemes[21,22] are the only existing pathway in LBM to reproduce Equation (1) within a parabolic level of accuracy, for any arbitrary shaped walls. Alternative LBM slip strategies either support the parabolic accuracy limited to lattice-aligned surfaces[34,36-39] or, otherwise, exhibit a degraded accuracy (lowering from second- to first-order) when applied to nonmesh aligned walls.[40-44] Still, despite the superior accuracy of the MR-based slip boundary schemes,[21,22] they carry a few points worthwhile improvement, namely: (i) nonlocality of implementation, for example, requiring at least two nodes to accommodate arbitrarily rotated parabolic solutions; (ii) inadequacy of the scheme to operate on edge/corner nodes due to the lack of neighboring nodes; and (iii) inherent difficulty to independently prescribe normal/tangential conditions in a linkwise manner.

The purpose of this work is to present an alternative LBM slip velocity boundary scheme that reproduces Equation (1) within a parabolic level of accuracy while, at the same time, relaxing some of the shortcomings listed above. Given that most of these shortcomings are intrinsic to the linkwise operation principle, the in-node principle is followed here. Figure 1 depicts a schematic representation of the differences between linkwise and in-node operation principles for a generic $\vec{x}_b$ boundary node.

The LBM implementation of the wall slip boundary condition, following this in-node operation principle, is based on the local second-order boundary (LSOB) scheme.[25,45-47] The LSOB technique was originally derived[25,45] for no-slip walls and, subsequently, extended to model the free-interface condition,[46] adopting a degraded "first-order" construction. Recently, the original LSOB procedure, for no-slip walls, was revisited[47] with focus on the following improvements: (i) reformulation of LSOB in a more convenient two-relaxation-time (TRT) symmetrized structure for the $D3Q19$ lattice; (ii) reassessment of the LSOB linear system construction and its effect on the method's support of the viscosity-independent numerical errors;[48] and (iii) comparison of the LSOB no-slip approach against state-of-the-art linkwise no-slip schemes.[26,28] The analysis here performed tightly follows that of the previous LSOB work,[47] extending those results towards the modeling of the slip velocity condition, Equation (1).

As application domain, we focus on the simulation of microchannel slip flows. While in the LBM context this benchmark has been largely studied for 2D channel geometries,[21,36-41,44] its extension to 3D ducts has received considerable less attention, apart from a few exceptions that modeled the slip condition on circular tubes[43] and rectangular ducts.[43,49] Unlike for no-slip walls, the assessment of convergence rates and other accuracy measures have been scarcely reported for slip-flow problems, particularly when the wall does not align with the LBM uniform Cartesian mesh,[21,41,42] much seldom in 3D domains. We address this question here by considering the discretization of distinct channel cross-sections with rectangular, triangular, circular and annular shapes. The obtained numerical results permit us to characterize the performance of the considered slip schemes and how they cope with LBM as a second-order solver for microchannel slip-flow problems.

The article is structured as follows. Section 2 presents the LBM basic nomenclature and the most pertinent formulae used in this work. Section 3 briefly revises the general boundary condition theory in LBM, describes the key steps of the LSOB algorithm and how it compares to other in-node boundary strategies. Sections 4 and 5 explain the formulation

of LSOB for the slip condition, Equation (1), illustrating its application for planar and curved boundaries, respectively. Section 6 reviews substitute linkwise strategies to prescribe the slip condition. Section 7 provides the numerical evaluation of the slip boundary schemes here considered for different microchannel geometries. Finally, Section 8 concludes the article with a summary of the main results.

2 | LATTICE BOLTZMANN METHOD

2.1 | Two-relaxation-time model

This work focuses on the LBM[29,31,32] with the two-relaxation-time (TRT) collision operator.[28,50] The TRT model formulates on the symmetry argument that any lattice quantity ψ_q can be decomposed into symmetric and anti-symmetric components as $\psi_q^+ = \frac{1}{2}(\psi_q + \psi_{\bar{q}})$ and $\psi_q^+ = \frac{1}{2}(\psi_q - \psi_{\bar{q}})$, where $\vec{c}_{\bar{q}} = -\vec{c}_q$ establishes a pair of anti-parallel discrete velocity $\vec{c}_q$, formed by one immobile $\vec{c}_0 = \vec{0}$ and $Q_m = Q - 1$ nonzero velocity vectors. On this basis, the evolution equation of the LBM-TRT scheme, with an external source S_q, is given by:

$$f_q(\vec{x} + \vec{c}_q, t+1) = \hat{f}_q(\vec{x}, t), \qquad q = 0, 1, \ldots, Q-1, \tag{3a}$$

$$\hat{f}_q(\vec{x}, t) = [f_q + \hat{n}_q^+ + \hat{n}_q^- + S_q^+ + S_q^-](\vec{x}, t), \qquad q = 0, 1, \ldots, Q_m/2, \tag{3b}$$

$$\hat{f}_{\bar{q}}(\vec{x}, t) = [f_{\bar{q}} + \hat{n}_q^+ - \hat{n}_q^- + S_q^+ - S_q^-](\vec{x}, t), \qquad q = 1, \ldots, Q_m/2. \tag{3c}$$

where f_q denotes the post-stream and $\hat{f}_q$ the post-collision state of the TRT populations, with the mass source $S_q^+ = 0$ and the momentum source $S_q^- = t_q^\star \; c_{q\alpha} \; F_\alpha$. Note, the external force term F_α is considered space-time constant here. Post-collision components $\hat{n}_q^\pm$ are defined as $\hat{n}_q^\pm := -n_q^\pm/\tau^\pm$, consisting of a rescaling of the nonequilibrium $n_q^\pm = (f_q^\pm - e_q^\pm)$, where $e_q^\pm$ denotes the (symmetric/anti-symmetric) equilibrium components, times the (symmetric/anti-symmetric) relaxation modes $\tau^\pm$. The associated relaxation eigenfunctions are defined as $\Lambda^\pm := \left(\tau^\pm - \frac{1}{2}\right)$. Note, $\Lambda^\pm$ are considered space-time constant in this work. Their product defines the key collision relaxation parameter $\Lambda := \Lambda^+\Lambda^-$, which controls the stationary field of nondimensional TRT solutions[48] at exact discrete level, that is, at all orders, beyond the second-order hydrodynamic limit.

Within TRT framework, the LBM populations can be *exactly* decomposed as:

$$f_q(\vec{x}, t) = \left[e_q^+ + e_q^- - \tau^+ \; \hat{n}_q^+ - \tau^- \; \hat{n}_q^-\right](\vec{x}, t). \tag{4}$$

This study is concerned with linear (Stokes) hydrodynamics where the equilibrium $e_q^\pm$ populations are given by:

$$e_q^+ = t_q^\star \; P, \tag{5a}$$

$$e_q^- = t_q^\star \; c_{q\alpha} \left(j_\alpha - \frac{1}{2} \; F_\alpha\right). \tag{5b}$$

Equation (5a) deals with pressure P, which relates to density ρ through the equation of state $P = c_s^2 \; \rho$, where c_s^2 is a free parameter, subject to stability bounds,[51] for example, $c_s^2 \in \left]0, \frac{3}{4}\right]$ for D3Q19. Equation (5b) deals with the fluid momentum j_α and the external body force F_α, where the index α denotes the components of these vector quantities. Equation (5) adopts hydrodynamic weights $t_q^\star$, which obey the required isotropic constraints $\sum_{q=1}^{Q-1} t_q^\star c_{q\alpha} c_{q\beta} = \delta_{\alpha\beta}$ and $\sum_{q=1}^{Q-1} t_q^\star \; c_{q\alpha} c_{q\beta} c_{q\gamma} c_{q\xi} = \frac{1}{3} \left(\delta_{\alpha\beta}\delta_{\gamma\xi} + \delta_{\alpha\gamma}\delta_{\beta\xi} + \delta_{\alpha\xi}\delta_{\beta\gamma}\right)$. The macroscopic fields appearing in the $e_q^\pm$ equilibria are determined by the discrete velocity moments:

$$\rho = \sum_{q=0}^{Q-1} f_q, \quad j_\alpha = \sum_{q=1}^{Q-1} f_q \; c_{q\alpha} + \frac{1}{2} \; F_\alpha, \quad F_\alpha = \sum_{q=1}^{Q-1} S_q^- \; c_{q\alpha}. \tag{6}$$

The conservation laws satisfied by f_q are established by the mass and momentum constraints on the nonequilibrium components:

$$\sum_{q=0}^{Q-1} \hat{n}_q^+ = 0, \quad \sum_{q=1}^{Q-1} \hat{n}_q^- c_{q\alpha} = 0. \tag{7}$$

2.2 | Chapman–Enskog steady-state approximations

The steady-state Chapman–Enskog expansion, developed up to the third order, displays the following relationship between the nonequilibrium populations $\hat{n}_q^\pm$ and the spatial derivatives of their $e_q^\pm$ equilibrium counterparts:[28,48,50]

$$\hat{n}_q^\pm = \partial_q e_q^\mp - \Lambda^\mp \, \partial_q^2 e_q^\pm - S_q^\pm + \mathcal{O}(\epsilon^3). \tag{8}$$

The residue $\mathcal{O}(\epsilon^3)$ in Equation (8) denotes the leading-order truncation of the approximation,[50] where ϵ represents the perturbation parameter of the asymptotic expansion.[29,31,52] In practice, ϵ defines the ratio of the lattice unit over a characteristic length scale $\mathcal{L}$, that is, $\epsilon \sim 1/\mathcal{L}$, where $\mathcal{L} := N \, \Delta x$ is a grid scale measure. Inserting Equation (8) into Equation (7), and performing a few algebraic manipulations revolving around the isotropic constraints of the discrete velocity set,[26] the content of $\hat{n}_q^+$ and $\hat{n}_q^-$ is recovered as follows:

$$\hat{n}_q^+ = t_q^\star \, \mathcal{H}^{(2)}_{q\alpha\beta} \, \partial_\beta \, j_\alpha + \mathcal{O}(\epsilon^3), \qquad \mathcal{H}^{(2)}_{q\alpha\beta} := c_{q\alpha} c_{q\beta} - \frac{1}{3}\delta_{\alpha\beta}, \tag{9a}$$

$$\hat{n}_q^- = -\Lambda^+ \, t_q^\star \, \mathcal{H}^{(3)}_{q\alpha\beta\gamma} \, \partial_{\beta\gamma} \, j_\alpha + \mathcal{O}(\epsilon^4), \qquad \mathcal{H}^{(3)}_{q\alpha\beta\gamma} := c_{q\alpha} c_{q\beta} c_{q\gamma} - \frac{1}{3}\left(c_{q\alpha} \, \delta_{\beta\gamma} + c_{q\beta} \, \delta_{\alpha\gamma} + c_{q\gamma} \, \delta_{\alpha\beta}\right). \tag{9b}$$

Equation (9b) is derived by starting with $\hat{n}_q^- = t_q^\star \, c_{q\alpha} \, (\partial_\alpha P - F_\alpha) - \Lambda^+ \, t_q^\star \, c_{q\alpha} c_{q\beta} c_{q\gamma} \, \partial_{\beta\gamma} \, j_\alpha + \mathcal{O}(\epsilon^4)$, which stems from the anti-symmetric component of Equation (8), and replacing $t_q^\star \, c_{q\alpha} \, (\partial_\alpha P - F_\alpha)$ by the lattice-projected momentum Laplacian, $t_q^\star \, c_{q\alpha} \, \nu \, \partial_{\beta\beta} j_\alpha$ following the bulk flow equations, Equation (10), subject to the incompressibility flow condition $\partial_\alpha j_\alpha = 0$. Accordingly, the introduction of Equation (9) into mass and momentum constraints, given by Equation (7), leads to the steady Stokes flow equations in bulk.

$$\partial_\alpha j_\alpha = 0, \quad \partial_\alpha P - F_\alpha = \nu \, \partial_\beta \left(\partial_\beta j_\alpha + \partial_\alpha j_\beta\right), \quad \nu = \frac{\Lambda^+}{3}. \tag{10}$$

Based on Von Karman's relationship, $\mathrm{Kn} \propto \frac{\mathrm{Ma}}{\mathrm{Re}}$, it follows that the slip-flow regime, $\mathrm{Kn} < 0.1$, under the slow flow assumption, $\mathrm{Re} \ll 1$, leads to the stronger requirement of flow incompressibility, that is, $\mathrm{Ma} \ll \mathrm{Re} \ll \mathrm{Kn}$. This scaling forms the basis of the slip-flow theory, rigorously formulated by Sone[16] in his asymptotic theory for slightly rarefied gases. A similar scaling relationship is followed in this work.

The extension of this study to compressible and moderate- or high-Reynolds number flows will be considered in a future contribution. The account of compressibility phenomena could be done by using the standard weakly compressible equilibrium model projected onto MRT basis, which permits disentangling the additional velocity divergence term from the LSOB first-order expansion, explicitly working out the mode controlled by the bulk viscosity eigenvalue.[46] The consideration of nonlinear effects in the matrix inversion problem of LSOB algorithm is also possible by adopting existing numerical strategies, such as linearization of momentum around a previous time-step solution[46] or via more advanced numerical procedures used in steady-state nonlinear LBM solvers[53,54]). Some of these approaches have been already applied to first-order LSOB schemes in the modeling of transient, nonlinear and compressible two-phase flows,[46] or highly nonlinear weakly compressible flows.[55]

Proceeding with the previously presented derivations, the "hydrodynamic content" of (post-stream) TRT populations, Equation (4), can be explicitly unfold, within the third-order accurate representation of the Chapman–Enskog expansion, Equation (8), as given by:

$$f_q = \underbrace{t_q^\star \, P}_{e_q^+} + \underbrace{t_q^\star \, c_{q\alpha} \left(j_\alpha - \frac{1}{2} \, F_\alpha\right)}_{e_q^-} - \tau^+ \underbrace{t_q^\star \, \mathcal{H}^{(2)}_{q\alpha\beta} \, \partial_\beta \, j_\alpha}_{\hat{n}_q^+ + \mathcal{O}(\epsilon^3)} + \tau^- \underbrace{\Lambda^+ \, t_q^\star \, \mathcal{H}^{(3)}_{q\alpha\beta\gamma} \, \partial_{\beta\gamma} \, j_\alpha}_{-\hat{n}_q^- + \mathcal{O}(\epsilon^4)}. \tag{11}$$

Hereinafter, when using this Equation (11), the leading error $\mathcal{O}(\epsilon^n)$ with $n \geq 3$ will be omitted to alleviate notation, though we highlight that its existence should not be forgotten, as this residue quantifies the accuracy of the f_q reconstruction process.

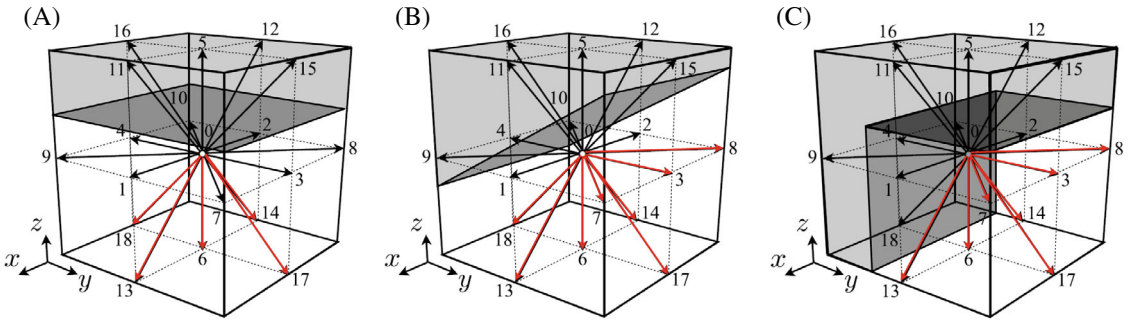

FIGURE 2 Examples of boundary node types for different wall discretizations on the $D3Q19$ computational cell. Unknown discrete velocities, denoting $f_q(\vec{x}_b) \in \mathcal{U}$ are marked in red. (A) Regular boundary node [$\dim(\mathcal{U}) = 5$]. (B) Singular boundary node [$\dim(\mathcal{U}) = 8$]. (C) Corner boundary node [$\dim(\mathcal{U}) = 7$] [Colour figure can be viewed at wileyonlinelibrary.com]

2.3 | Application to channel-type problems

Let us address the modeling of a steady slow viscous flow bounded by walls of arbitrary shape where the slip velocity condition, Equation (1), holds. In doing so, let us consider the following flow field characteristics: (i) the momentum solution $\vec{j}$ aligns along the x-axis; (ii) there are negligible variations along the streamwise flow direction (or zero in case of periodicity) $\vec{\nabla} \cdot \vec{e}_x = \partial_x = 0$, so that $\vec{j} = j_x(y,z)\,\vec{e}_x$; and (iii) the flow driving mechanisms can be attributed to a constant body-force density $\vec{F} = F_x\,\vec{e}_x$ or an equivalent negative pressure-gradient $-\vec{\nabla}P = -\partial_x P\,\vec{e}_x$. Under these circumstances, considering the $D3Q19$ lattice,[29-32,56] see Figure 2, the reconstruction of TRT populations given by Equation (11) is expressed as follows:

$$f_q = t_q^\star \left(P + c_{qx}\left(j_x - \frac{1}{2}F_x\right) - \tau^+ \left(\mathcal{H}^{(2)}_{qxy}\,\partial_y j_x + \mathcal{H}^{(2)}_{qxz}\,\partial_z j_x\right) + \tau^-\,\Lambda^+ \left(\mathcal{H}^{(3)}_{qxyy}\,\partial_{yy} j_x + \mathcal{H}^{(3)}_{qxzz}\,\partial_{zz} j_x\right)\right), \tag{12}$$

where the Hermite polynomial bases, first introduced in Equation (9), are here explicitly given by

$$\mathcal{H}^{(2)}_{qxy} = c_{qx}c_{qy}, \quad \mathcal{H}^{(2)}_{qxz} = c_{qx}c_{qz}, \quad \mathcal{H}^{(3)}_{qxyy} = \left(c_{qy}^2 - \frac{1}{3}\right)c_{qx}, \quad \mathcal{H}^{(3)}_{qxzz} = \left(c_{qz}^2 - \frac{1}{3}\right)c_{qx}. \tag{13}$$

In D3Q19 model the lattice weights are $t_q^\star = \{t^I, t^{II}\} = \{\frac{1}{6}, \frac{1}{12}\}$, respectively, for the first (cardinal) and the second (diagonal) neighbor link, and the immobile weight can be defined as $t_0^\star = c_s^{-2} - \sum_{q=1}^{Q_m} t_q^\star$; or equivalently $t_0^\star = e_0/(c_s^2\,\rho)$, with the rest equilibrium population determined as $e_0 = \rho - \sum_{q=1}^{Q} e_q^+$.

It must be stressed that derivations leading to Equation (12) can be easily extended to more general flow scenarios. For instance, Equation (12) could cover arbitrary flow orientations simply by re-expressing Equation (12) in the local streamline-oriented coordinate system $\vec{e}_{x'} = \cos\theta\,\vec{e}_x + \sin\theta\,\vec{e}_y$, so that $\vec{j} = j_{x'}(y,z)\,\vec{e}_{x'}$; in fact, in the original LSOB formulation[25] this general rotated frame notation was adopted; it is omitted here since only horizontal flows ($\theta = 0$) are considered. Additionally, the streamwise flow invariance condition could also be released, by handling terms such as $\partial_{x'} j_{x'}$ in the very same way as $\partial_{y'} j_{x'}$; here, only the later are accounted for, due to their dominant role in the channel flow problem class. Finally, the inclusion of spatially nonuniform body force terms could also be considered, by following the ideas already developed in previous works;[57,58] though, this task is beyond the scope of the present work. In the next section, we address the reconstruction of Equation (12) following the algorithm known as the LSOB scheme.[25,45,47]

3 | BOUNDARY CONDITIONS IN LBM

3.1 | Definitions

Standard LBM runs on a uniform Cartesian mesh. As a result, the discretization of solid geometries intrinsically brings in three types of computational nodes:[31] (i) *Solid nodes* which are sites outside the fluid domain; (ii) *fluid nodes* which are sites where the LBM update rule, Equation (3), applies; and (iii) *boundary nodes* $\vec{x}_b$ which are sites also belonging to the fluid region, but with at least one link connected to the outside solid domain, that is, $\vec{x}_b + \vec{c}_q \in$ solid. At boundary

nodes there are populations which are entering from the outside domain that are unknown. To differentiate them it is convenient to separate the boundary populations into two sets:

$$\mathcal{K} = \{q \mid f_q \text{ is known}\}, \quad \mathcal{U} = \{q \mid f_q \text{ is unknown}\}, \tag{14}$$

whereby $\dim(\mathcal{K}) + \dim(\mathcal{U}) = Q$. Here, rather than considering Q, only Q_m populations are necessary since focus is given to steady flows, where the rest population f_0 does not need to be considered for incompressible flows.

The closure of the LBM boundary value problem consists in prescribing adequate values for $f_q(\vec{x}_b)$ with $q \in \mathcal{U}$ that guarantee: (i) an accurate reproduction of the hydrodynamic boundary condition and (ii) a "smooth" transition between boundary and bulk solutions. The failure of any of these conditions gives rise to very specific defects. Point (i), the misrepresentation of the boundary condition, will create artificial jumps between numerical and physical boundary solutions, while point (ii), the mismatch between populations moving across boundary and bulk nodes, will induce artificial accommodation layers,[25,59-62] which may distort the intended solution everywhere. The goal of the LBM boundary schemes presented in this work is to cope with these two conditions as accurately as possible in implementing Equation (1).

3.2 | LSOB algorithm

According to the general exposition given in Section 3.1, the key idea of the LSOB methodology is to reconstruct the unknown boundary populations, $f_q(\vec{x}_b)$ with $q \in \mathcal{U}$, using the "second-order" approximation expressed by Equation (11). Along these lines, the boundary-value closure problem for $f_q(\vec{x}_b)$ reduces to determining the hydrodynamic fields and their derivatives.

The distinctive element of the LSOB algorithm is that it proposes to locally determine those derivatives, that is, $\partial_\beta j_\alpha$ and $\partial_{\beta\gamma} j_\alpha$ in Equation (11), by searching for their values with the help of the known boundary information. In the TRT framework, they are readily available through the content of each nonequilibrium component $\hat{n}_q^+(\vec{x}_b)$ and $\hat{n}_q^-(\vec{x}_b)$, according to Equation (9).

After having determined the momentum derivatives, the boundary node momentum itself, $\vec{j}(\vec{x}_b)$, can be computed with the help of the wall boundary condition—in this case the slip velocity condition, Equation (1)—based on a Taylor series type condition, where the expansion increment δ_n measures the distance between the boundary node and the wall, $\delta_n = (\vec{x}_b - \vec{x}_w) \cdot \vec{n}$. In consistency with the $\mathcal{O}(\epsilon^3)$ error in the $f_q(\vec{x}_b)$ reconstruction, this Taylor expansion is truncated to second-order, that is, with $\mathcal{O}(\delta x^3)$ residue. As will be explained in this article, the Taylor-type approximation of the wall boundary condition can be realized in two ways,[25,45,47] either by operating with node or wall variables. Each strategy is, accordingly, termed as Lnode or Lwall and their explicit formulations will be presented in Sections 4 and 5, for the cases of planar and curved walls, respectively.

Finally, the $f_q(\vec{x}_b)$ reconstruction problem is closed with the prescription of the pressure boundary value $P(\vec{x}_b)$, which can be locally determined by adapting well-established algorithms.[25,63] At $\vec{x}_b$ the zeroth-order mass moment is split as $\frac{P}{c_s^2} = \sum_{q\in\mathcal{K}} f_q + \sum_{q\in\mathcal{U}} f_q$ and the part of f_q belonging to the $\mathcal{U}$ set is subject to the LSOB approximation, yielding $P(\vec{x}_b) = \frac{1}{c_s^{-2} - \sum_{q\in\mathcal{U}} t_q^\star} \left[\sum_{q\in\mathcal{K}} f_q(\vec{x}_b) + (\vec{j}(\vec{x}_b) - \frac{1}{2}\vec{F}) \cdot \sum_{q\in\mathcal{U}} t_q^\star \, \vec{c}_q - \tau^+ \sum_{q\in\mathcal{U}} \hat{n}_q^+(\vec{x}_b) - \tau^- \sum_{q\in\mathcal{U}} \hat{n}_q^-(\vec{x}_b) \right]$.

3.3 | LSOB evolution and comparisons to other in-node boundary schemes

The in-node philosophy of prescribing boundary conditions in LBM, as illustrated in Figure 1, has produced many schemes. Since a lot of them have close connections with the LSOB approach, next we will briefly review the historical development of the LSOB together with those schemes that borrowed some features from its algorithm.

The idea to reconstruct the unknown incoming boundary populations, that is, $f_q(\vec{x}_b)$ with $q \in \mathcal{U}$, based on the second-order Chapman–Enskog approximation, as given by Equation (11), was originally proposed in the work of Ginzburg,[64] using finite-differences (FD) approximations to construct the first and second momentum derivatives. At the same time, Skordos[65] proposed a similar reconstruction procedure, but restricted to a "first-order" representation of Equation (11), with the first momentum derivative computed through FD. However, in both cases, the use of FD approximations led to specific drawbacks, such as making the algorithm nonlocal and mainly suitable for straight walls.[25,64]

To overcome those limitations, the LSOB scheme[25,45] was subsequently derived as a local approach to reconstruct the unknown populations, that is, $f_q(\vec{x}_b)$ with $q \in \mathcal{U}$, but without having to resort to FDs. Its distinctive idea was to extract the unknown hydrodynamic fields from the known boundary populations, that is, $f_q(\vec{x}_b)$ with $q \in \mathcal{K}$. This procedure is justified under the assumption that both known and unknown boundary populations follow a similar structure, given by Equation (11). More than 25 years after the original publication,[25] the LSOB idea was revived[47] with the twofold purpose of reformulating its algorithm to cope with the beneficial proprieties of the LBM-TRT model and applying it to a broader range of problem classes, as described in Section 1.

During the aforementioned 25 years period, a number of related in-node boundary schemes has been proposed, partially inspired in the ideas of the LSOB approach. As a common feature, they all considered degraded reconstructions of the boundary populations, Equation (11), limited to the first-order Chapman–Enskog approximation. As a distinct feature, they proposed alternate procedures to determine the required first-order derivatives at the boundary node. On the one hand, the works by Halliday et al.,[66] Hollis et al.,[67] and Dorschner et al.[68] proposed using FD approximations, while Verschaeve and Müller[69] and Mohammadipour et al.[70] proposed the use of finite element interpolations. On the other hand, the works of Zou and He,[63] Junk and Yang,[71] Latt and Malaspinas,[72,73] Verschaeve,[74] and Zhang et al.[55] proposed resorting to the information from the known boundary populations, while Noble et al.,[75] Bennet et al.,[76] and Krastins et al.[77] opted to work with the moments. Additional information on the implementation, accuracy and stability characteristics of these in-node boundary schemes can be found in the very comprehensive analyses[72,78,79] dedicated to this subject. It is worth noticing that, among the in-node boundary schemes listed here, only a few[55,68-71] addressed the modeling of boundaries of general shape, that is, solid walls (either planar or curved) not aligning with the LBM uniform mesh.

4 | LSOB SLIP SCHEME ON PLANAR WALLS

Plane surfaces are conveniently described in a *Cartesian coordinate system*. Here, we consider both fixed (y, z) and rotated (y', z') coordinate frames, the two relating as $y' = y\ \cos\theta + z\ \sin\theta$ and $z' = -y\ \sin\theta + z\ \cos\theta$. The y'- and z'-components align with wall tangent and wall normal vectors, respectively. Next, we will describe the Lnode and Lwall formulations for the slip velocity condition on planar walls together with implementation examples.

4.1 | Lnode slip scheme

In the Lnode approach the flow field $\vec{j} = j_x\vec{e}_x$ is evaluated on "node coordinates," which are conveniently represented on the fixed coordinate system (y, z). The key element of the Lnode approach consists in the approximation of the unknown momentum $j_x(\vec{x}_b)$ in Equation (12) that is replaced by its wall counterpart representation $j_x(\vec{x}_w)$ through the second-order Taylor series development along the wall-normal direction:

$$\begin{aligned} j_x(\vec{x}_b) &= j_x(\vec{x}_w) + \delta_{z'}\ \partial_{z'} j_x(\vec{x}_b) - \frac{\delta_{z'}^2}{2}\ \partial_{z'z'} j_x(\vec{x}_b) \\ &= j_x^{\text{wall}}(\vec{x}_w) + (\delta_{z'} + C\ \lambda_{z'})\left(-\sin\theta\ \partial_y j_x(\vec{x}_b) + \cos\theta\ \partial_z j_x(\vec{x}_b)\right) \\ &\quad - \left(\frac{\delta_{z'}^2}{2} + C\ \lambda_{z'}\ \delta_{z'}\right)\left(\sin^2\theta\ \partial_{yy} j_x(\vec{x}_b) + \cos^2\theta\ \partial_{zz} j_x(\vec{x}_b) - \sin 2\theta\ \partial_{yz} j_x(\vec{x}_b)\right), \end{aligned} \tag{15}$$

with coefficients

$$\delta_{z'} := \delta_n\ n_{z'} \text{ with } \delta_n = (\vec{x}_b - \vec{x}_w)\cdot\vec{n} \text{ and } \lambda_{z'} := \lambda\ n_{z'} \text{ with } \lambda = \text{Kn}\ D_h. \tag{16}$$

Above, $n_{z'} = \vec{n}\cdot\vec{e}_{z'}$ denotes the projection of the inward unitary normal vector $\vec{n}$ on the $\vec{e}_{z'}$ component of the (y', z') system; since the z' -axis is, by definition, aligned with the wall normal, then $n_{z'}$ takes either 1 or -1 values. The derivation of Equation (15) is performed in three steps. First, the fluid momentum at the wall $j_x(\vec{x}_w)$ is equated to the slip velocity boundary condition $j_x(\vec{x}_w) = j_x^{\text{wall}}(\vec{x}_w) + C\ \lambda_{z'}\ \partial_{z'} j_x(\vec{x}_w)$. Second, the momentum derivative existing here is recast to node coordinates by Taylor expanding it as $\partial_{z'} j_x(\vec{x}_w) = \partial_{z'} j_x(\vec{x}_b) - \delta_{z'}\ \partial_{z'z'} j_x(\vec{x}_b)$. Third, the end result is remapped from the rotated wall-oriented frame (y', z') onto the fixed Cartesian system (y, z).

The Lnode reconstruction of $f_q(\vec{x}_b)$ with $q \in \mathcal{U}$ is obtained by the substitution of Equation (15) into Equation (12), which reads:

$$\begin{aligned}\frac{f_q(\vec{x}_b)}{t_q^\star} &= P(\vec{x}_b) + c_{qx}\left(j_x^{\text{wall}}(\vec{x}_w) - \frac{1}{2}F_x\right)\\ &+\left(-(\delta_{z'} + C\,\lambda_{z'})\sin\theta\; c_{qx} - \tau^+\,\mathcal{H}^{(2)}_{qxy}\right)\partial_y j_x(\vec{x}_b) + \left((\delta_{z'} + C\,\lambda_{z'})\cos\theta\; c_{qx} - \tau^+\,\mathcal{H}^{(2)}_{qxz}\right)\partial_z j_x(\vec{x}_b)\\ &+\left(-\left(\frac{\delta^2_{z'}}{2} + C\,\lambda_{z'}\,\delta_{z'}\right)\sin^2\theta\; c_{qx} + \tau^-\,\Lambda^+\,\mathcal{H}^{(3)}_{qxyy}\right)\partial_{yy} j_x(\vec{x}_b)\\ &+\left(-\left(\frac{\delta^2_{z'}}{2} + C\,\lambda_{z'}\,\delta_{z'}\right)\cos^2\theta\; c_{qx} + \tau^-\,\Lambda^+\,\mathcal{H}^{(3)}_{qxzz}\right)\partial_{zz} j_x(\vec{x}_b) + \left(\left(\frac{\delta^2_{z'}}{2} + C\,\lambda_{z'}\,\delta_{z'}\right)\sin 2\theta\; c_{qx}\right)\partial_{yz} j_x(\vec{x}_b).\end{aligned} \tag{17}$$

Equation (17) is self-consistent with the original Lnode no-slip scheme,[47] that is $\lim \lambda \to 0$ in Equation (17) recovers the Eq. (4.2) of the no-slip work.[47]

Overall, the problem of reconstructing $f_q(\vec{x}_b)$ with $q \in \mathcal{U}$ boils down to determining the nonequilibrium hydrodynamic fields in Equation (17), which can be grouped in the following set:

$$\mathcal{X} = \{\partial_y j_x(\vec{x}_b), \partial_z j_x(\vec{x}_b), \partial_{yy} j_x(\vec{x}_b), \partial_{zz} j_x(\vec{x}_b), \partial_{yz} j_x(\vec{x}_b)\}^\intercal. \tag{18}$$

According to the LSOB main idea, the elements of $\mathcal{X}$ can be extracted through the content of the nonequilibrium populations $\hat{n}_q^\pm$, which in approximated form are given by Equation (9). In Lnode formalism this relationship takes the following explicit form:

$$\frac{\hat{n}_q^+(\vec{x}_b)}{t_q^\star} = \mathcal{H}^{(2)}_{qxy}\,\partial_y j_x(\vec{x}_b) + \mathcal{H}^{(2)}_{qxz}\,\partial_z j_x(\vec{x}_b), \tag{19a}$$

$$-\frac{1}{\Lambda^+}\frac{\hat{n}_q^-(\vec{x}_b)}{t_q^\star} = \mathcal{H}^{(3)}_{qxyy}\,\partial_{yy} j_x(\vec{x}_b), + \mathcal{H}^{(3)}_{qxzz}\,\partial_{zz} j_x(\vec{x}_b) \tag{19b}$$

that can be recast in matrix form as:

$$\underbrace{\begin{bmatrix}\hat{n}_q^+/t_q^\star\\ -\hat{n}_q^-/(\Lambda^+\,t_q^\star)\end{bmatrix}}_{\mathcal{N}} = \underbrace{\begin{bmatrix}\mathcal{H}^{(2)}_{qxy} & \mathcal{H}^{(2)}_{qxz} & 0 & 0 & 0\\ 0 & 0 & \mathcal{H}^{(3)}_{qxyy} & \mathcal{H}^{(3)}_{qxzz} & 0\end{bmatrix}}_{[\mathbf{M}]}\underbrace{\begin{bmatrix}\partial_y j_x(\vec{x}_b)\\ \partial_z j_x(\vec{x}_b)\\ \partial_{yy} j_x(\vec{x}_b)\\ \partial_{zz} j_x(\vec{x}_b)\\ \partial_{yz} j_x(\vec{x}_b)\end{bmatrix}}_{\mathcal{X}},$$

where $\mathcal{N}$ is a vector formed by the known populations, the matrix $[\mathbf{M}]$ is formed by the coefficients arising in the LSOB decomposition of the aforementioned populations, Equation (12), and $\mathcal{X}$ is the vector formed by the unknown momentum derivatives at $\vec{x}_b$. According to this representation, the content of $\mathcal{X}$ is locally determined through the solution of the linear algebra problem:

$$\mathcal{X} = [\mathbf{M}]^{-1}\mathcal{N}. \tag{20}$$

4.1.1 | Implementation of Lnode scheme

Regular boundary nodes

Consider the $D3Q19$ discretization of the *horizontal* plane wall illustrated in Figure 2A, where $\dim(\mathcal{U}) = 5$. This is a regular node where the number of independent equations available is always equal or greater than the number of unknowns, that is, $\text{rank}[\mathbf{M}] \geq \dim(\mathcal{X})$, this way Equation (19) can be solved through a linear algebra problem. The matrix construction can use 3 independent (nontrivial) populations: 1 coordinate population $\rightarrow$ (referring to link $c_{qx} = \pm 1$ with $c_{qy} = c_{qz} = 0$) and 2 diagonal populations $\searrow$ (referring to link $c_{qx}c_{qy} = \pm 1$) and $\nearrow$ (referring to link $c_{qx}c_{qz} = \pm 1$). The Lnode

formulation may be written as a system composed of all these populations or a subset containing just two of them. For the horizontal wall displayed in Figure 2A, a sufficient subset can be formed with the $\searrow$ and $\nearrow$ populations, that is:

$$\underbrace{\begin{bmatrix} \hat{n}^{+}_{\searrow}/t^{II} \\ \hat{n}^{+}_{\nearrow}/t^{II} \\ -\hat{n}^{-}_{\searrow}/(\Lambda^{+}\ t^{II}) \\ -\hat{n}^{-}_{\nearrow}/(\Lambda^{+}\ t^{II}) \end{bmatrix}}_{\mathcal{N}} = \underbrace{\begin{bmatrix} \mathcal{H}^{(2)}_{\searrow xy} & \mathcal{H}^{(2)}_{\searrow xz} & 0 & 0 \\ \mathcal{H}^{(2)}_{\nearrow xy} & \mathcal{H}^{(2)}_{\nearrow xz} & 0 & 0 \\ 0 & 0 & \mathcal{H}^{(3)}_{\searrow xyy} & \mathcal{H}^{(3)}_{\searrow xzz} \\ 0 & 0 & \mathcal{H}^{(3)}_{\nearrow xyy} & \mathcal{H}^{(3)}_{\nearrow xzz} \end{bmatrix}}_{[\mathbf{M}]} \underbrace{\begin{bmatrix} \partial_y j_x(\vec{x}_b) \\ \partial_z j_x(\vec{x}_b) \\ \partial_{yy} j_x(\vec{x}_b) \\ \partial_{zz} j_x(\vec{x}_b) \end{bmatrix}}_{\mathcal{X}}.$$

When the Lnode approach is operated with the full population set then $[\mathbf{M}]$ becomes a rectangular matrix. In this case, the solution of Equation (20) is determined by its pseudo-inverse,[45-47] which can be computed through standard numerical programming techniques, such as the singular value decomposition (SVD).[47] After determining the unknown momentum derivatives, by solving Equation (20), the problem is finally closed with the insertion of $\mathcal{X}$ into $f_q(\vec{x}_b)$ with $q \in \mathcal{U}$, as given by Equation (17).

For instance, consider the top planar wall illustrated in Figure 2A. The unknown boundary populations $c_{qx}c_{qy} = 0$ and $c_{qx}c_{qz} = \pm 1$ that stream in from the horizontal wall ($\theta = \pi$) are reconstructed as:

$$\begin{aligned} \frac{f_q(\vec{x}_b)}{t^{\star}_q} &= P(\vec{x}_b) + c_{qx}\left(j_x^{\text{wall}}(\vec{x}_w) - \frac{1}{2}\,F_x\right) \\ &+ \left(-(\delta_{z'} + C\ \lambda_{z'})\ c_{qx} - \tau^{+}\ \mathcal{H}^{(2)}_{qxz}\right)\partial_z j_x(\vec{x}_b) + \left(-\left(\frac{\delta^2_{z'}}{2} + C\ \lambda_{z'}\ \delta_{z'}\right)\ c_{qx} + \tau^{-}\ \Lambda^{+}\ \mathcal{H}^{(3)}_{qxzz}\right)\partial_{zz} j_x(\vec{x}_b). \end{aligned} \tag{21}$$

Singular boundary nodes

Consider the $D3Q19$ discretization of the *inclined* plane wall illustrated in Figure 2B, where $\dim(\mathcal{U}) = 8$. Here, the original system used for the "regular node" case leads to $\text{rank}[\mathbf{M}] > \dim(\mathcal{X})$, resulting in an under-determined system. To make it determined, the conditions set by Equation (19) must be augmented. Following the works,[45,47] we propose including the derivatives of the known wall tangent momentum condition along the boundary, whose validity is discussed below, after Equation (23). For a uniform momentum on the flat wall surface, we can write the following two extra constraints:

$$\begin{cases} \partial_{y'} j_x(\vec{x}_w) - C\ \lambda_{z'}\ \partial_{y'z'} j_x(\vec{x}_w) = \partial_{y'} j_x(\vec{x}_b) - (\delta_{z'} + C\ \lambda_{z'})\ \partial_{y'z'} j_x(\vec{x}_b) \\ \qquad\qquad = \left(\cos\theta\ \partial_y j_x(\vec{x}_b) + \sin\theta\ \partial_z j_x(\vec{x}_b)\right) \\ \qquad\qquad - (\delta_{z'} + C\ \lambda_{z'})\left(\frac{1}{2}\sin 2\theta\ (-\partial_{yy} j_x(\vec{x}_b) + \partial_{zz} j_x(\vec{x}_b)) + \cos 2\theta\ \partial_{yz} j_x(\vec{x}_b)\right) = 0 \\ \partial_{y'y'} j_x(\vec{x}_w) = \cos^2\theta\ \partial_{yy} j_x(\vec{x}_b) + \sin^2\theta\ \partial_{zz} j_x(\vec{x}_b) + \sin 2\theta\ \partial_{yz} j_x(\vec{x}_b) = 0. \end{cases} \tag{22}$$

In matrix form, the linear algebra formulation at "singular nodes" is set by combining Equation (22) with Equation (19), reading:

$$\underbrace{\begin{bmatrix} \hat{n}^{+}_{\rightarrow}/t^{I} \\ \hat{n}^{+}_{\searrow}/t^{II} \\ \hat{n}^{+}_{\nearrow}/t^{II} \\ -\hat{n}^{-}_{\rightarrow}/(\Lambda^{+}\ t^{I}) \\ -\hat{n}^{-}_{\searrow}/(\Lambda^{+}\ t^{II}) \\ -\hat{n}^{-}_{\nearrow}/(\Lambda^{+}\ t^{II}) \\ 0 \\ 0 \end{bmatrix}}_{\mathcal{N}} = \underbrace{\begin{bmatrix} \mathcal{H}^{(2)}_{\rightarrow xy} & \mathcal{H}^{(2)}_{\rightarrow xz} & 0 & 0 & 0 \\ \mathcal{H}^{(2)}_{\searrow xy} & \mathcal{H}^{(2)}_{\searrow xz} & 0 & 0 & 0 \\ \mathcal{H}^{(2)}_{\nearrow xy} & \mathcal{H}^{(2)}_{\nearrow xz} & 0 & 0 & 0 \\ 0 & 0 & \mathcal{H}^{(3)}_{\rightarrow xyy} & \mathcal{H}^{(3)}_{\rightarrow xzz} & 0 \\ 0 & 0 & \mathcal{H}^{(3)}_{\searrow xyy} & \mathcal{H}^{(3)}_{\searrow xzz} & 0 \\ 0 & 0 & \mathcal{H}^{(3)}_{\nearrow xyy} & \mathcal{H}^{(3)}_{\nearrow xzz} & 0 \\ \cos\theta & \sin\theta & \frac{1}{2}(\delta_{z'} + C\ \lambda_{z'})\ \sin 2\theta & -\frac{1}{2}(\delta_{z'} + C\ \lambda_{z'})\sin 2\theta & -(\delta_{z'} + C\ \lambda_{z'})\cos 2\theta \\ 0 & 0 & \cos^2\theta & \sin^2\theta & \sin 2\theta \end{bmatrix}}_{[\mathbf{M_h}]} \underbrace{\begin{bmatrix} \partial_y j_x(\vec{x}_b) \\ \partial_z j_x(\vec{x}_b) \\ \partial_{yy} j_x(\vec{x}_b) \\ \partial_{zz} j_x(\vec{x}_b) \\ \partial_{yz} j_x(\vec{x}_b) \end{bmatrix}}_{\mathcal{X}}.$$

Following Equation (20), the unknown momentum derivatives are then determined as:

$$\mathcal{X} = [\mathbf{M_h}]^{-1}\mathcal{N}. \tag{23}$$

In case $[\mathbf{M_h}]$ is rectangular then $[\mathbf{M_h}]^{-1}$ represents its pseudo-inverse, which can be easily computed using, for example, SVD or least-square methods.[45-47] Finally, the problem is closed with the insertion of $\mathcal{X}$ into $f_q(\vec{x}_b)$ with $q \in \mathcal{U}$, as given by Equation (17).

Concerning the validity of Equation (22) on boundaries obeying the slip velocity condition, it is important to stress that it only holds true for constant slip flows. In case $\partial_{y'}\left(j_x(\vec{x}_w) - C\ \lambda_{z'}\ \partial_{z'} j_x(\vec{x}_w)\right) \neq 0$, the proposed condition can be easily generalized and modified with the inclusion of other solution fields, which are easily accessible due to the explicit manner they are treated here. This contrasts with linkwise boundary schemes where the slip condition is set implicitly[21,22] so that the attempt to independently modify each component of the momentum or its derivative along a specific link may become a cumbersome task.[27]

Corner boundary nodes

Consider the $D3Q19$ discretization of the *corner* geometry illustrated in Figure 2C, where $\dim(\mathcal{U}) = 7$. The "corner node" problem is treated similarly to the "regular node" case, despite its larger number of unknowns. The linear independency of the system $\mathcal{N} = [\mathbf{M}]\mathcal{X}$ is guaranteed by considering that, for each wall meeting the corner, different momentum derivatives will be used in the reconstruction of $f_q(\vec{x}_b)$ with $q \in \mathcal{U}$. These differences come from the particular Taylor series approximations of $j_x(\vec{x}_b)$, Equation (15), where specific momentum derivatives appear along each wall normal direction, and are then applied to the reconstruction of the respective populations.

For instance, consider the rectangular corner illustrated in Figure 2C. The momentum derivatives are obtained by inverting:

$$\underbrace{\begin{bmatrix} \hat{n}^+_{\searrow}/t^{II} \\ \hat{n}^+_{\nearrow}/t^{II} \\ -\hat{n}^-_{\searrow}/(\Lambda^+\ t^{II}) \\ -\hat{n}^-_{\nearrow}/(\Lambda^+\ t^{II}) \end{bmatrix}}_{\mathcal{N}} = \underbrace{\begin{bmatrix} \mathcal{H}^{(2)}_{\searrow xy} & \mathcal{H}^{(2)}_{\searrow xz} & 0 & 0 \\ \mathcal{H}^{(2)}_{\nearrow xy} & \mathcal{H}^{(2)}_{\nearrow xz} & 0 & 0 \\ 0 & 0 & \mathcal{H}^{(3)}_{\searrow xyy} & \mathcal{H}^{(3)}_{\searrow xzz} \\ 0 & 0 & \mathcal{H}^{(3)}_{\nearrow xyy} & \mathcal{H}^{(3)}_{\nearrow xzz} \end{bmatrix}}_{[\mathbf{M}]} \underbrace{\begin{bmatrix} \partial_y j_x(\vec{x}_b) \\ \partial_z j_x(\vec{x}_b) \\ \partial_{yy} j_x(\vec{x}_b) \\ \partial_{zz} j_x(\vec{x}_b) \end{bmatrix}}_{\mathcal{X}}.$$

Then, the unknown boundary populations $c_{qx}c_{qy} = \pm 1$ and $c_{qx}c_{qz} = 0$ that stream in from the vertical wall ($\theta = \pi/2$) are reconstructed as:

$$\begin{aligned} \frac{f_q(\vec{x}_b)}{t^\star_q} &= P(\vec{x}_b) + c_{qx}\left(j_x^{\text{wall}}(\vec{x}_w) - \frac{1}{2}\ F_x\right) \\ &+ \left(-(\delta_{z'} + C\ \lambda_{z'})\ c_{qx} - \tau^+\ \mathcal{H}^{(2)}_{qxy}\right)\partial_y j_x(\vec{x}_b) + \left(-\left(\frac{\delta^2_{z'}}{2} + C\ \lambda_{z'}\ \delta_{z'}\right)\ c_{qx} + \tau^-\ \Lambda^+\ \mathcal{H}^{(3)}_{qxyy}\right)\partial_{yy} j_x(\vec{x}_b). \end{aligned} \tag{24}$$

The unknown boundary populations $c_{qx}c_{qy} = 0$ and $c_{qx}c_{qz} = \pm 1$ that stream in from the horizontal wall ($\theta = \pi$) are reconstructed exactly as given in Equation (21) for a top planar wall. Finally, the reconstruction of the unknown boundary populations $c_{qx}c_{qy} \pm 0$ and $c_{qx}c_{qz} = \pm 1$ that stream in along the link that crosses the corner ($\theta = n\ \frac{\pi}{4}$ with $n \in \mathbb{Z}$) follow similar lines.

Other types of boundary nodes

The three types of node configurations described above cover the main situations encountered in the discretization of duct flows. Although more complicated cases may arise at very particular discretization scenarios, for example, isolated nodes surrounded by walls bounding all directions except along one link, such cases can be addressed in a similar fashion, for example, by combining the "singular" and "corner" systems, namely by adding the surface-known information for all adjacent walls. A potential alternative approach may use the combination of different approaches, for example, LSOB and MR, or even the degrade of accuracy, for example, using lower-order boundary schemes, at these very particular sites, as was exemplified in previous works.[28,60]

4.2 | Lwall slip scheme

In the Lwall approach the flow field $\vec{j} = j_x \vec{e}_x$ is evaluated on "wall coordinates," which are more conveniently represented on the rotated coordinate system (y', z') that locally aligns with the wall surface, with y'- and z'-components being parallel to wall tangent and wall normal vectors. The key element of the Lwall approach consists in replacing both the unknown momentum and the momentum derivatives, defined at boundary node $\vec{x}_b$, by their wall values, set at $\vec{x}_w$, with the help of the second-order Taylor series approximations:

$$\begin{cases} j_x(\vec{x}_b) = j_x(\vec{x}_w) + \delta_{z'}\partial_{z'}j_x(\vec{x}_w) + \frac{\delta_{z'}^2}{2}\partial_{z'z'}j_x(\vec{x}_w) \\ \qquad\quad = j_x^{\text{wall}}(\vec{x}_w) + (\delta_{z'} + C\,\lambda_{z'})\,\partial_{z'}j_x(\vec{x}_w) + \frac{\delta_{z'}^2}{2}\partial_{z'z'}j_x(\vec{x}_w) \\ \partial_{y'}j_x(\vec{x}_b) = \partial_{y'}j_x(\vec{x}_w) + \delta_{z'}\,\partial_{y'z'}j_x(\vec{x}_w) \\ \qquad\quad = (\delta_{z'} + C\,\lambda_{z'})\,\partial_{y'z'}j_x(\vec{x}_w) \\ \partial_{z'}j_x(\vec{x}_b) = \partial_{z'}j_x(\vec{x}_w) + \delta_{z'}\,\partial_{z'z'}j_x(\vec{x}_w) \\ \partial_{y'y'}j_x(\vec{x}_b) = \cancel{\partial_{y'y'}j_x(\vec{x}_w)} \\ \partial_{z'z'}j_x(\vec{x}_b) = \partial_{z'z'}j_x(\vec{x}_w) \end{cases} \tag{25}$$

with coefficients

$$\delta_{z'} := \delta_n\, n_{z'} \text{ with } \delta_n = (\vec{x}_b - \vec{x}_w)\cdot\vec{n} \text{ and } \lambda_{z'} := \lambda\, n_{z'} \text{ with } \lambda = \text{Kn}\, D_h, \tag{26}$$

where $n_{z'} = \vec{n}\cdot\vec{e}_{z'}$ that may take either 1 or -1 values, depending on whether the vector $\vec{n}$ and $\vec{e}_{z'}$ are parallel or antiparallel (recall, $\vec{n}$ points inward the fluid domain). Here, $j_x^{\text{wall}}(\vec{x}_w)$ denotes the wall "momentum." The wall slip condition is used in the approximation of the fluid momentum $j_x(\vec{x}_w) = j_x^{\text{wall}}(\vec{x}_w) + C\,\lambda_{z'}\,\partial_{z'}j_x(\vec{x}_w)$ and its derivative $\partial_{y'}j_x(\vec{x}_w) = C\,\lambda_{z'}\,\partial_{y'z'}j_x(\vec{x}_w)$. The vanishing of term $\partial_{y'y'}j_x(\vec{x}_w) = 0$ follows from the assumption of uniform flow momentum over the wall tangent plane, which can be justified under the constant slip hypothesis. The explicit enforcement of these wall conditions on the reconstruction of the boundary populations is an intrinsic feature of the Lwall formulation[25] and the key reason to express the derivatives at $\vec{x}_w$, as in Equation (25). This contrasts with the Lnode approach, where similar conditions involving the momentum derivatives on the wall are only brought up at "singular nodes," through the constraints given by Equation (22).

The Lwall reconstruction of $f_q(\vec{x}_b)$ with $q \in \mathcal{U}$ is obtained by substituting Equation (25) into Equation (12), which reads:

$$\begin{aligned} \frac{f_q(\vec{x}_b)}{t_q^\star} &= P(\vec{x}_b) + c_{qx}\left(j_x^{\text{wall}}(\vec{x}_w) - \frac{1}{2}F_x\right) + \left((\delta_{z'} + C\,\lambda_{z'})\;c_{qx} - \tau^+\,\mathcal{H}^{(2)}_{qxz'}\right)\partial_{z'}j_x(\vec{x}_w) \\ &+ \left(\frac{\delta_{z'}^2}{2}\,c_{qx} - \tau^+\,\delta_{z'}\,\mathcal{H}^{(2)}_{qxz'} + \tau^-\,\Lambda^+\left(\mathcal{H}^{(3)}_{qxyy}\sin^2\theta + \mathcal{H}^{(3)}_{qxzz}\cos^2\theta\right)\right)\partial_{z'z'}j_x(\vec{x}_w) \\ &+ \left(-\tau^+\;(\delta_{z'} + C\,\lambda_{z'})\;\mathcal{H}^{(2)}_{qxy'} + \tau^-\,\Lambda^+\left(\mathcal{H}^{(3)}_{qxzz} - \mathcal{H}^{(3)}_{qxyy}\right)\sin 2\theta\right)\partial_{y'z'}j_x(\vec{x}_w), \end{aligned} \tag{27}$$

where $\mathcal{H}^{(2)}_{qxy'} = c_{qx}c_{qy'}$ and $\mathcal{H}^{(2)}_{qxz'} = c_{qx}c_{qz'}$ with $c_{qy'} = c_{qy}\cos\theta + c_{qz}\sin\theta$ and $c_{qz'} = -c_{qy}\sin\theta + c_{qz}\cos\theta$.

Equation (27) is self-consistent with the original Lwall no-slip scheme,[47] as $\lim \lambda \to 0$ in Equation (27) leads to Equation (4.6) of the no-slip work.[47]

The problem of reconstructing $f_q(\vec{x}_b)$ with $q \in \mathcal{U}$ is reduced to the problem of determining the nonequilibrium hydrodynamic fields in Equation (27), which collectively are given by the set:

$$\mathcal{X} = \{\partial_{z'}j_x(\vec{x}_w), \partial_{z'z'}j_x(\vec{x}_w), \partial_{y'z'}j_x(\vec{x}_w)\}^\intercal. \tag{28}$$

Note, compared to the Lnode approach, Equation (18), the size of $\mathcal{X}$ in Lwall is two elements smaller.

The elements of $\mathcal{X}$ are readily available, within the TRT framework, by accessing to the content of the nonequilibrium populations $\hat{n}_q^\pm$. Simplified to this case, the application of Equation (9) in the Lwall approach reads:

$$\frac{\hat{n}_q^+(\vec{x}_b)}{t_q^\star} = \mathcal{H}^{(2)}_{qxz'}\left(\partial_{z'} j_x(\vec{x}_w) + \delta_{z'}\ \partial_{z'z'} j_x(\vec{x}_w)\right) + (\delta_{z'} + C\ \lambda_{z'})\ \mathcal{H}^{(2)}_{qxy'}\ \partial_{y'z'} j_x(\vec{x}_w), \tag{29a}$$

$$-\frac{1}{\Lambda^+}\frac{\hat{n}_q^-(\vec{x}_b)}{t_q^\star} = \left(\mathcal{H}^{(3)}_{qxyy}\sin^2\theta + \mathcal{H}^{(3)}_{qxzz}\cos^2\theta\right)\ \partial_{z'z'} j_x(\vec{x}_w) - \left(\mathcal{H}^{(3)}_{qxyy} - \mathcal{H}^{(3)}_{qxzz}\right)\sin 2\theta\ \partial_{y'z'} j_x(\vec{x}_w), \tag{29b}$$

which can be recast in matrix form as follows:

$$\underbrace{\begin{bmatrix} \hat{n}_q^+/t_q^\star \\ -\hat{n}_q^-/(\Lambda^+\ t_q^\star)\end{bmatrix}}_{\mathcal{N}} = \underbrace{\begin{bmatrix} \mathcal{H}^{(2)}_{qxz'} & \delta_{z'}\ \mathcal{H}^{(2)}_{qxz'} & (\delta_{z'} + C\ \lambda_{z'})\ \mathcal{H}^{(2)}_{qxy'} \\ 0 & \left(\mathcal{H}^{(3)}_{qxyy}\sin^2\theta + \mathcal{H}^{(3)}_{qxzz}\cos^2\theta\right) & -\left(\mathcal{H}^{(3)}_{qxyy} - \mathcal{H}^{(3)}_{qxzz}\right)\sin 2\theta \end{bmatrix}}_{[\mathbf{M}]} \underbrace{\begin{bmatrix} \partial_{z'} j_x(\vec{x}_w) \\ \partial_{z'z'} j_x(\vec{x}_w) \\ \partial_{y'z'} j_x(\vec{x}_w)\end{bmatrix}}_{\mathcal{X}}.$$

The unknown momentum derivatives at $\vec{x}_w$ are locally determined through the solution of the linear algebra problem, Equation (20). Unlike the Lnode system formulation, in the Lwall approach the matrix [**M**] must be square in order to preserve the parameterization structure of the TRT solution in bulk. The verification of this property can be checked by confirming that the steady-state TRT solution supports viscosity-independent numerical errors.

In the Lwall formulation two discretization scenarios can be identified: (i) the general case where the wall stands arbitrarily inclined with respect to the mesh and (ii) the degenerated case where the wall aligns with the lattice. They are discussed next.

4.2.1 | Implementation of Lwall scheme

Mesh aligned horizontal/vertical plane wall (degenerated case)

Consider the $D3Q19$ discretization of the *horizontal* plane wall illustrated in Figure 2A, where $\dim(\mathcal{U}) = 5$. Given that $\theta = \pi$, the formulation of the linear algebra system, Equation (29), degenerates to:

$$\underbrace{\begin{bmatrix} \hat{n}^+_{\nearrow}/t^{II} \\ -\hat{n}^-_{\nearrow}/(\Lambda^+\ t^{II})\end{bmatrix}}_{\mathcal{N}} = \underbrace{\begin{bmatrix} -\mathcal{H}^{(2)}_{\nearrow xz} & -\delta_{z'}\ \mathcal{H}^{(2)}_{\nearrow xz} \\ 0 & \mathcal{H}^{(3)}_{\nearrow xzz}\end{bmatrix}}_{[\mathbf{M}]} \underbrace{\begin{bmatrix} \partial_z j_x(\vec{x}_w) \\ \partial_{zz} j_x(\vec{x}_w)\end{bmatrix}}_{\mathcal{X}}.$$

After finding $\mathcal{X} = [\mathbf{M}]^{-1}\mathcal{N}$ we can reconstruct $f_q(\vec{x}_b)$ with $q \in \mathcal{U}$. This way, the unknown boundary populations $c_{qx}c_{qy} = 0$ and $c_{qx}c_{qz} = \pm 1$ that stream in from the horizontal wall ($\theta = \pi$) are reconstructed as:

$$\begin{aligned}\frac{f_q(\vec{x}_b)}{t_q^\star} = P(\vec{x}_b) + c_{qx}\left(j_x^{\text{wall}}(\vec{x}_w) - \frac{1}{2}F_x\right) + \left((\delta_{z'} + C\ \lambda_{z'})\ c_{qx} + \tau^+\ \mathcal{H}^{(2)}_{qxz}\right)\partial_z j_x(\vec{x}_w) \\ + \left(\frac{\delta^2_{z'}}{2}\ c_{qx} + \tau^+\ \delta_{z'}\ \mathcal{H}^{(2)}_{qxz} + \tau^-\ \Lambda^+\ \mathcal{H}^{(3)}_{qxzz}\right)\partial_{zz} j_x(\vec{x}_w).\end{aligned} \tag{30}$$

With the procedure shown above, only two components of the same nontrivial population are involved in the Lwall application in horizontal or vertical plane walls. Yet, it is worth pointing out that such an approach is not unique. In this degenerated configuration the term $\partial_{yz} j_x(\vec{x}_w)$ could also be extracted from $\hat{n}_q^+(\vec{x}_b)$, by including the $\mathcal{H}^{(2)}_{\searrow xy}$ projection into [**M**]. In that case, the determinacy of the Lwall system would require the inclusion of three components of two linearly independent populations, for example, $\mathcal{N} = \{\hat{n}^+_{\nearrow}, \hat{n}^-_{\nearrow}, \hat{n}^+_{\searrow}\}$. In practice, however, this procedure proves unnecessary since the term $\partial_{yz} j_x(\vec{x}_w)$ is not used in the Lwall reconstruction of $f_q(\vec{x}_b)$ with $q \in \mathcal{U}$, as shown in Equation (30).

Mesh oblique plane wall (arbitrary wall orientation)

Consider the $D3Q19$ discretization of the *inclined* plane wall illustrated in Figure 2B, where $\dim(\mathcal{U}) = 8$. Noticeably, the Lwall approach does not fall into the Lnode system indeterminacy. Rather, a linearly independent [**M**] system can always

be constructed to determine $\mathcal{X}$ since rank[$\mathbf{M}$] $\geq$ dim($\mathcal{X}$) = 3 under all possible discretization scenarios considered here. For general plane wall discretizations, that is, where the degenerated case $\theta = n\,\frac{\pi}{4}$ with $n \in \mathbb{Z}$ in the yz-plane does not occur, the Lwall formulation reads as follows:

$$\underbrace{\begin{bmatrix} \hat{n}^{+}_{\nearrow}/t^{II} \\ -\hat{n}^{-}_{\rightarrow}/(\Lambda^{+}\ t^{I}) \\ -\hat{n}^{-}_{\nearrow}/(\Lambda^{+}\ t^{II}) \end{bmatrix}}_{\mathcal{N}} = \underbrace{\begin{bmatrix} \mathcal{H}^{(2)}_{\nearrow xz'} & \delta_{z'}\ \mathcal{H}^{(2)}_{\nearrow xz'} & \delta_{z'}\ \mathcal{H}^{(2)}_{\nearrow xy'} \\ 0 & \left(\mathcal{H}^{(3)}_{\rightarrow xyy}\sin^2\theta + \mathcal{H}^{(3)}_{\rightarrow xzz}\cos^2\theta\right) & \left(\mathcal{H}^{(3)}_{\rightarrow xzz} - \mathcal{H}^{(3)}_{\rightarrow xyy}\right)\sin 2\theta \\ 0 & \left(\mathcal{H}^{(3)}_{\nearrow xyy}\sin^2\theta + \mathcal{H}^{(3)}_{\nearrow xzz}\cos^2\theta\right) & \left(\mathcal{H}^{(3)}_{\nearrow xzz} - \mathcal{H}^{(3)}_{\nearrow xyy}\right)\sin 2\theta \end{bmatrix}}_{[\mathbf{M}]} \underbrace{\begin{bmatrix} \partial_{z'}j_x(\vec{x}_w) \\ \partial_{z'z'}j_x(\vec{x}_w) \\ \partial_{y'z'}j_x(\vec{x}_w) \end{bmatrix}}_{\mathcal{X}}.$$

At *corner boundary nodes* the Lwall implements quite alike the Lnode approach. The main difference is that in the Lwall case two independent systems are constructed to permit the determination of two distinct $\mathcal{X}$ solutions, rather than a common $\mathcal{X}$ solution as in Lnode. This separation helps distinguishing the components of $\mathcal{X}$ at different walls, which is necessary to avoid possible ambiguities from the wall-oriented rotated system (y', z'). On this basis, each of the computed solutions $\mathcal{X} = [\mathbf{M}]^{-1}\mathcal{N}$ is applied to the reconstruction of the corresponding wall crossing populations $f_q(\vec{x}_b)$ with $q \in \mathcal{U}$, via Equation (27). In the particular case the incoming population pertains to a link crossing the corner then its reconstruction involves the mean value from the two $\mathcal{X}$ solution sets.

5 | LSOB SLIP SCHEME ON CURVED WALLS

Curved surfaces are conveniently described in a curvilinear coordinate frame. Bearing in mind that generalizations to other cases are straightforward, we focus here on a *cylindrical coordinate system* (r, θ), where $y = r\ \cos\theta$ and $z = r\ \sin\theta$, with the axis origin, $r = 0$, centered at the middle pipe coordinate (y_0, z_0). As LBM populations rest on a Cartesian frame the mapping $(r, \theta) \mapsto (y, z)$ shall be undertaken. Next, the Lnode and Lwall formulations are presented for this case.

5.1 | Lnode slip scheme

Similarly to the plane wall case, it is convenient to work on the fixed coordinate frame (y, z). The Lnode approach replaces the unknown momentum $j_x(\vec{x}_b)$ in Equation (12) by its wall momentum counterpart $j_x(\vec{x}_w)$ with the help of the second-order Taylor series approximation:

$$\begin{aligned} j_x(\vec{x}_b) &= j_x(\vec{x}_w) + \delta_r\,\partial_r j_x(\vec{x}_b) - \frac{\delta_r^2}{2}\,\partial_{rr} j_x(\vec{x}_b) \\ &= j_x^{\text{wall}}(\vec{x}_w) + \left(\delta_r\left(1 + \frac{\delta_r}{2r}\right) + C\,\lambda_r\left(1 + \frac{\delta_r}{r}\right)\right)\left(\cos\theta\,\partial_y j_x(\vec{x}_b) + \sin\theta\,\partial_z j_x(\vec{x}_b)\right) \\ &\quad - \left(\frac{\delta_r^2}{2} + C\,\lambda_r\,\delta_r\right)\left(\partial_{yy}u_x(\vec{x}_b) + \partial_{zz}u_x(\vec{x}_b)\right) + \cancel{\frac{\delta_r^2}{2r^2}\,\partial_{\theta\theta}u_x(\vec{x}_b)}, \end{aligned} \tag{31}$$

where $r = \sqrt{(y_b - y_0)^2 + (z_b - z_0)^2}$ is the radial location of the boundary node $\vec{x}_b$ and the coefficients are

$$\delta_r := \delta_n\ n_r \text{ with } \delta_n = (\vec{x}_b - \vec{x}_w)\cdot\vec{n} \text{ and } \lambda_r := \lambda\ n_r \text{ with } \lambda = \text{Kn}\ D_h \tag{32}$$

with $n_r = \vec{n}\cdot\vec{e}_r$ denoting the projection of the inward unitary normal vector $\vec{n}$ on the $\vec{e}_r$ component of the (r, θ) system; since the r -axis is, by definition, aligned with the wall normal, then n_r takes either 1 or -1 values. Here, $j_x^{\text{wall}}(\vec{x}_w)$ is the wall "momentum." Implicitly, the condition $\partial_{\theta\theta}j_x(\vec{x}_b) = 0$ is used, which follows from the second-order Taylor series approximation $\partial_{\theta\theta}j_x(\vec{x}_b) = \partial_{\theta\theta}j_x(\vec{x}_w)$ applied to the uniform surface momentum condition $\partial_{\theta\theta}j_x(\vec{x}_w) = 0$, see Equation (34). Equation (30) is derived in three steps by: (i) invoking the slip velocity boundary condition $j_x(\vec{x}_w) = j_x^{\text{wall}}(\vec{x}_w) + C\ \lambda_r\ \partial_r j_x(\vec{x}_w)$; (ii) re-expressing the derivative in node coordinates as $\partial_r j_x(\vec{x}_w) = \partial_r j_x(\vec{x}_b) - \delta_r\ \partial_{rr} j_x(\vec{x}_b)$; and (iii) remapping the result from the polar (r, θ) to the Cartesian (y, z) coordinate system.

The Lnode reconstruction of $f_q(\vec{x}_b)$ with $q \in \mathcal{U}$ is obtained by substituting Equation (30) into Equation (12), which reads:

$$\begin{aligned}\frac{f_q(\vec{x}_b)}{t_q^\star} &= P(\vec{x}_b) + c_{qx}\left(j_x^{\text{wall}}(\vec{x}_w) - \frac{1}{2}F_x\right)\\ &+\left(\left(\delta_r\left(1+\frac{\delta_r}{2r}\right)+C\ \lambda_r\left(1+\frac{\delta_r}{r}\right)\right)\cos\theta\ c_{qx} - \tau^+\ \mathcal{H}^{(2)}_{qxy}\right)\partial_y j_x(\vec{x}_b)\\ &+\left(\left(\delta_r\left(1+\frac{\delta_r}{2r}\right)+C\ \lambda_r\left(1+\frac{\delta_r}{r}\right)\right)\sin\theta\ c_{qx} - \tau^+\ \mathcal{H}^{(2)}_{qxz}\right)\partial_z j_x(\vec{x}_b)\\ &+\left(-\left(\frac{\delta_r^2}{2}+C\ \lambda_r\ \delta_r\right)\ c_{qx} + \tau^-\ \Lambda^+\ \mathcal{H}^{(3)}_{qxyy}\right)\partial_{yy} j_x(\vec{x}_b)\\ &+\left(-\left(\frac{\delta_r^2}{2}+C\ \lambda_r\ \delta_r\right)\ c_{qx} + \tau^-\ \Lambda^+\ \mathcal{H}^{(3)}_{qxzz}\right)\partial_{zz} j_x(\vec{x}_b).\end{aligned} \tag{33}$$

The no-slip condition is recovered as $\lim_{\lambda\to 0}$ Equation (33), which matches Eq. (5.2) derived in a previous no-slip work.[47] The set of the unknown fields in Equation (33), represented as $\mathcal{X}$ is given by Equation (18); hence, the elements of $\mathcal{X}$ are extracted from the very same linear algebra system established by the $\hat{n}_q^{\pm}$ populations presented in Equation (19). The only difference appears in the treatment of *singular boundary nodes*; here, the hydrodynamically based extra constraints are found by differentiating the known wall tangent momentum condition along the curved wall surface:

$$\begin{cases}\partial_\theta j_x(\vec{x}_w) - C\ \lambda_r\ \partial_{\theta r} j_x(\vec{x}_w) = \partial_\theta j_x(\vec{x}_b) - (\delta_r + C\ \lambda_r)\ \partial_{\theta r} j_x(\vec{x}_b)\\ \qquad = (r - \delta_r + C\ \lambda_r)(-\sin\theta\ \partial_y j_x(\vec{x}_b) + \cos\theta\ \partial_z j_x(\vec{x}_b))\\ \qquad\quad - r\ (\delta_r + C\ \lambda_r)\left(\frac{1}{2}\sin 2\theta\ (-\partial_{yy} j_x(\vec{x}_b) + \partial_{zz} j_x(\vec{x}_b)) + \cos 2\theta\ \partial_{yz} j_x(\vec{x}_b)\right) = 0,\\ \partial_{\theta\theta} j_x(\vec{x}_w) = -r\ \left(\cos\theta\ \partial_y j_x(\vec{x}_b) + \sin\theta\ \partial_z j_x(\vec{x}_b)\right)\\ \qquad\quad + r^2\ \left(\sin^2\theta\ \partial_{yy} j_x(\vec{x}_b) + \cos^2\theta\ \partial_{zz} j_x(\vec{x}_b) - \sin 2\theta\ \partial_{yz} j_x(\vec{x}_b)\right) = 0.\end{cases} \tag{34}$$

When the constraints (Equation 34) are used, it augments the set $\mathcal{X}$, featuring the unknowns given by Equation (18).

5.2 | Lwall slip scheme

The application of Lwall to curved walls does not benefit from the adoption of a rotated frame (y', z') (or any specific curvilinear system as discussed in Reference 47). Therefore, we keep the simplest fixed Cartesian frame (y, z). The approximation of the momentum and the momentum derivatives between $\vec{x}_b$ and $\vec{x}_w$ are expressed by the second-order Taylor series developments, given as follows:

$$\begin{cases} j_x(\vec{x}_b) = j_x(\vec{x}_w) + \delta_r\,\partial_r j_x(\vec{x}_w) + \frac{\delta_r^2}{2}\,\partial_{rr} j_x(\vec{x}_w)\\ \quad = j_x(\vec{x}_w) + \delta_r\left(1 - \frac{\delta_r}{2R}\right)\left(\cos\theta\,\partial_y j_x(\vec{x}_w) + \sin\theta\,\partial_z j_x(\vec{x}_w)\right)\\ \quad\quad + \frac{\delta_r^2}{2}\left(\partial_{yy} j_x(\vec{x}_w) + \partial_{zz} j_x(\vec{x}_w)\right) - \frac{\delta_r^2}{2R^2}\cancel{\partial_{\theta\theta} j_x(\vec{x}_w)},\\ \partial_y j_x(\vec{x}_b) = \partial_y j_x(\vec{x}_w) + \delta_r\,\partial_{ry} j_x(\vec{x}_w)\\ \quad = \partial_y j_x(\vec{x}_w) + \delta_r\left(\cos\theta\,\partial_{yy} j_x(\vec{x}_w) + \sin\theta\,\partial_{yz} j_x(\vec{x}_w)\right),\\ \partial_z j_x(\vec{x}_b) = \partial_z j_x(\vec{x}_w) + \delta_r\,\partial_{rz} j_x(\vec{x}_w)\\ \quad = \partial_z j_x(\vec{x}_w) + \delta_r\left(\cos\theta\,\partial_{yz} j_x(\vec{x}_w) + \sin\theta\,\partial_{zz} j_x(\vec{x}_w)\right),\\ \partial_{yy} j_x(\vec{x}_b) = \partial_{yy} j_x(\vec{x}_w),\\ \partial_{zz} j_x(\vec{x}_b) = \partial_{zz} j_x(\vec{x}_w),\end{cases} \tag{35}$$

where $R = \sqrt{(y_w - y_0)^2 + (z_w - z_0)^2}$ is the radius of the circular wall surface and the coefficients are

$$\delta_r := \delta_n \; n_r \text{ with } \delta_n = (\vec{x}_b - \vec{x}_w) \cdot \vec{n} \text{ and } \lambda_r := \lambda \; n_r \text{ with } \lambda = \text{Kn} \; D_h, \tag{36}$$

with $n_r = \vec{n} \cdot \vec{e}_r$ that may take either 1 or −1 values, depending on whether the vectors $\vec{n}$ and $\vec{e}_r$ are parallel or antiparallel (recall, $\vec{n}$ points inward the fluid domain). Above, $j_x^{\text{wall}}(\vec{x}_w)$ is the wall "momentum." The wall slip condition is accounted for only in the approximation of the fluid momentum $j_x(\vec{x}_w) = j_x^{\text{wall}}(\vec{x}_w) + C \; \lambda_r \; \partial_r j_x(\vec{x}_w)$. The simplification $\partial_{\theta\theta} j_x(\vec{x}_w) = 0$ is justified under the constant slip flow condition, previously employed in Equation (34). Unlike the plane wall case, the Lwall formulations on curved surfaces does not reduce the size of $\mathcal{X}$ as conditions $\partial_\theta j_x(\vec{x}_w) = 0$ and $\partial_{\theta\theta} j_x(\vec{x}_w) = 0$ do not fit naturally into the structure of f_q populations. Hence, for curved surfaces, operating on "wall coordinates" only partially simplifies the final result.

The Lwall reconstruction of $f_q(\vec{x}_b)$ with $q \in \mathcal{U}$ is obtained by substituting Equation (34) into Equation (12), which reads:

$$\begin{aligned}
\frac{f_q(\vec{x}_b)}{t_q^\star} = {} & P(\vec{x}_b) + c_{qx} \left(j_x^{\text{wall}}(\vec{x}_w) - \frac{1}{2} F_x \right) \\
& + \left(\left(\delta_r \left(1 - \frac{\delta_r}{2R} \right) + C \; \lambda_r \right) \cos\theta \; c_{qx} - \tau^+ \; \mathcal{H}_{qxy}^{(2)} \right) \partial_y j_x(\vec{x}_w) \\
& + \left(\left(\delta_r \left(1 - \frac{\delta_r}{2R} \right) + C \; \lambda_r \right) \sin\theta \; c_{qx} - \tau^+ \; \mathcal{H}_{qxz}^{(2)} \right) \partial_z j_x(\vec{x}_w) \\
& + \left(\frac{\delta_r^2}{2} \; c_{qx} - \tau^+ \; \delta_r \; \mathcal{H}_{qxy}^{(2)} \; \cos\theta + \tau^- \; \Lambda^+ \; \mathcal{H}_{qxyy}^{(3)} \right) \partial_{yy} j_x(\vec{x}_w) \\
& + \left(\frac{\delta_r^2}{2} \; c_{qx} - \tau^+ \; \delta_r \; \mathcal{H}_{qxz}^{(2)} \; \sin\theta + \tau^- \; \Lambda^+ \; \mathcal{H}_{qxzz}^{(2)} \right) \partial_{zz} j_x(\vec{x}_w) \\
& + \left(-\tau^+ \; \delta_r \left(\mathcal{H}_{qxy}^{(2)} \; \sin\theta + \mathcal{H}_{qxz}^{(2)} \; \cos\theta \right) \right) \partial_{yz} j_x(\vec{x}_w).
\end{aligned} \tag{37}$$

The problem of determining the unknowns $\mathcal{X}$ in the reconstruction of Equation (37) is worked out by accessing to the content of $\hat{n}_q^\pm$ populations. Simplified to this case, the application of Equation (9) within the Lwall approach reads:

$$\begin{aligned}
\frac{\hat{n}_q^+(\vec{x}_b)}{t_q^\star} = {} & \left(\mathcal{H}_{qxy}^{(2)} \; \partial_y j_x(\vec{x}_w) + \mathcal{H}_{qxz}^{(2)} \; \partial_z j_x(\vec{x}_w) \right) \\
& + \delta_r \left(\mathcal{H}_{qxy}^{(2)} \; \cos\theta \; \partial_{yy} j_x(\vec{x}_w) + \mathcal{H}_{qxz}^{(2)} \; \sin\theta \; \partial_{zz} j_x(\vec{x}_w) + \left(\mathcal{H}_{qxy}^{(2)} \; \sin\theta + \mathcal{H}_{qxz}^{(2)} \; \cos\theta \right) \; \partial_{yz} j_x(\vec{x}_w) \right),
\end{aligned} \tag{38a}$$

$$-\frac{1}{\Lambda^+} \frac{\hat{n}_q^-(\vec{x}_b)}{t_q^\star} = \mathcal{H}_{qxyy}^{(3)} \partial_{yy} j_x(\vec{x}_w) + \mathcal{H}_{qxzz}^{(3)} \partial_{zz} j_x(\vec{x}_w), \tag{38b}$$

which can be recast in matrix form as:

$$\underbrace{\begin{bmatrix} \hat{n}_q^+ / t_q^\star \\ -\hat{n}_q^- / (\Lambda^+ \; t_q^\star) \end{bmatrix}}_{\mathcal{N}} = \underbrace{\begin{bmatrix} \mathcal{H}_{qxy}^{(2)} & \mathcal{H}_{qxz}^{(2)} & \delta_r \; \mathcal{H}_{qxy}^{(2)} \cos\theta & \delta_r \; \mathcal{H}_{qxz}^{(2)} \sin\theta & \left(\mathcal{H}_{qxy}^{(2)} \sin\theta + \mathcal{H}_{qxz}^{(2)} \cos\theta \right) \\ 0 & 0 & \mathcal{H}_{qxyy}^{(3)} & \mathcal{H}_{qxzz}^{(3)} & 0 \end{bmatrix}}_{[\mathbf{M}]} \underbrace{\begin{bmatrix} \partial_y j_x(\vec{x}_w) \\ \partial_z j_x(\vec{x}_w) \\ \partial_{yy} j_x(\vec{x}_w) \\ \partial_{zz} j_x(\vec{x}_w) \\ \partial_{yz} j_x(\vec{x}_w) \end{bmatrix}}_{\mathcal{X}}.$$

The unknown momentum derivatives at $\vec{x}_w$ are locally determined from the solution of the linear algebra problem set by Equation (20). Given that, when formulated on curved walls $\dim(\mathcal{X})$ is identical either in Lwall or in Lnode, the application of the Lwall approach on curved walls needs to distinguish between *regular* and *singular boundary nodes* similarly to Lnode.

The system shown above applies to *regular boundary nodes*. Though, this system can be further enriched by additionally including the constraint $\partial_{\theta\theta} j_x(\vec{x}_w) = 0$. The solution of $\mathcal{N} = [\mathbf{M}]\ \mathcal{X}$ augmented with this single constraint tends to provide more accurate solutions, while still being compatible with the TRT bulk parameterization.

In *singular boundary nodes*, the linear algebra system must be enlarged with the two extra constraints, based on the uniformity of the fluid momentum over the curved tangent surface:

$$\begin{cases} \partial_\theta j_x(\vec{x}_w) - C\ \lambda_r \partial_{r\theta} j_x(\vec{x}_w) = (R - C\ \lambda_r)\left(-\sin\theta\ \partial_y j_x(\vec{x}_w) + \cos\theta\ \partial_z j_x(\vec{x}_w)\right) \\ \qquad\qquad - C\ \lambda_r\ R\left(\frac{1}{2}\sin 2\theta\left(-\partial_{yy} j_x(\vec{x}_w) + \partial_{zz} j_x(\vec{x}_w)\right) + \cos 2\theta\ \partial_{yz} j_x(\vec{x}_w)\right) = 0, \\ \partial_{\theta\theta} j_x(\vec{x}_w) = -R\ \left(\cos\theta\ \partial_y j_x(\vec{x}_w) + \sin\theta\ \partial_z j_x(\vec{x}_w)\right) \\ \qquad\qquad + R^2\ \left(\sin^2\theta\ \partial_{yy} j_x(\vec{x}_w) + \cos^2\theta\ \partial_{zz} j_x(\vec{x}_w) - \sin 2\theta\ \partial_{yz} j_x(\vec{x}_w)\right) = 0. \end{cases} \tag{39}$$

The linear algebra formulation of Equation (38) including the constraints given by Equation (39) takes the following matrix form:

$$\underbrace{\begin{bmatrix} \hat{n}_q^+ / t_q^\star \\ -\hat{n}_q^- / (\Lambda^+\ t_q^\star) \\ 0 \\ 0 \end{bmatrix}}_{\mathcal{N}} = \underbrace{\begin{bmatrix} \mathcal{H}^{(2)}_{qxy} & \mathcal{H}^{(2)}_{qxz} & \delta_r\ \mathcal{H}^{(2)}_{qxy}\ \cos\theta & \delta_r\ \mathcal{H}^{(2)}_{qxz}\ \sin\theta & \left(\mathcal{H}^{(2)}_{qxy}\ \sin\theta + \mathcal{H}^{(2)}_{qxz}\ \cos\theta\right) \\ 0 & 0 & \mathcal{H}^{(3)}_{qxyy} & \mathcal{H}^{(3)}_{qxzz} & 0 \\ -(R - C\ \lambda_r)\ \sin\theta & (R - C\ \lambda_r)\ \cos\theta & \frac{1}{2} C\ \lambda_r\ R \sin 2\theta & -\frac{1}{2} C\ \lambda_r\ R \sin 2\theta & -C\ \lambda_r\ R \cos 2\theta \\ -R\ \cos\theta & -R\ \sin\theta & R^2\ \sin^2\theta & R^2\ \cos^2\theta & -R^2\ \sin 2\theta \end{bmatrix}}_{[\mathbf{M_h}]} \underbrace{\begin{bmatrix} \partial_y j_x(\vec{x}_w) \\ \partial_z j_x(\vec{x}_w) \\ \partial_{yy} j_x(\vec{x}_w) \\ \partial_{zz} j_x(\vec{x}_w) \\ \partial_{yz} j_x(\vec{x}_w) \end{bmatrix}}_{\mathcal{X}}.$$

6 | LINKWISE SLIP SCHEMES

Linkwise (directional) boundary schemes prescribe the unknown incoming boundary populations through the linear combination of other known populations lying on the same link direction. Along these lines, the boundary node $\vec{x}_b$, the solid node $\vec{x}_b + \delta_q\ \vec{c}_q$ and the nearest fluid node $\vec{x}_b - \vec{c}_q$ all belong to the same link direction; with convention $\vec{c}_{\overline{q}} = -\vec{c}_q$ so that the pair $\{\vec{c}_q, \vec{c}_{\overline{q}}\}$ is referred to as a link. Based on this connectivity, the general linkwise boundary update rule can be considered:[26-28]

$$\begin{aligned} f_{\overline{q}}(\vec{x}_b, t+1) = {} & \kappa_1 \tilde{f}_q(\vec{x}_b, t) + \overline{\kappa}_{-1} \tilde{f}_{\overline{q}}(\vec{x}_b, t) + \kappa_0 f_q(\vec{x}_b, t+1) \\ & + \kappa_{-1} f_q(\vec{x}_b - \vec{c}_q, t+1) + \overline{\kappa}_{-2} \tilde{f}_{\overline{q}}(\vec{x}_b - \vec{c}_q, t) \\ & + F_q^{p.c.}(\vec{x}_b, t) - \alpha^{(u)} j_q^{\text{wall}}(\vec{x}_w, t), \end{aligned} \tag{40}$$

where $\{\kappa_1, \kappa_0, \overline{\kappa}_{-1}, \kappa_{-1}, \overline{\kappa}_{-2}\}$ are interpolation coefficients, further supplemented by the term $F_q^{p.c.}$ and the scale prefactor $\alpha^{(u)}$ of the Dirichlet value $j_q^{\text{wall}} = t_q^\star\ (\vec{c}_q \cdot \vec{j}_{\text{wall}})$, where $\vec{j}_{\text{wall}}$ is the wall "momentum." Table 1 details the form of these terms for the three different classes of linkwise slip boundary schemes considered in this work,[21,22] namely: kinetic, linear, and parabolic schemes; in a self-consistent manner, they all reduce to well-known no-slip formulas when the slippage

TABLE 1 Linkwise slip boundary schemes: Coefficients of interpolation together with correction parameters $F_q^{p.c.}$ and $\alpha^{(u)}$ in Equation (40), where coefficients are $\alpha_q^+ := \left(\delta_q + C\ \lambda_q\right)$ and $\alpha_q^- := \left(\frac{\delta_q^2}{2} + C\ \lambda_q\ \delta_q\right)$

	Kinetic schemes (local)	Linear schemes (local)			Parabolic schemes (nonlocal)
	DBB	CLI slip	MGULI slip	MGDLI slip	MR1 slip
κ_1	$\frac{3\nu - C\lambda}{3\nu + C\lambda}$	1	$2\alpha_q^+$	$\frac{1}{2\alpha_q^+}$	1
κ_0	0	$\frac{1-2\alpha_q^+}{1+2\alpha_q^+}$	$1-\kappa_1$	0	$\frac{1-2\alpha_q^+-4\alpha_q^-}{1+2\alpha_q^++2\alpha_q^-}$
$\overline{\kappa}_{-1}$	0	$-\kappa_0$	0	$1-\kappa_1$	$-\kappa_0$
κ_{-1}	0	0	0	0	$\frac{2\alpha_q^-}{1+2\alpha_q^++2\alpha_q^-}$
$\overline{\kappa}_{-2}$	0	0	0	0	$-\kappa_{-1}$
$\alpha^{(u)}$	$2\ \kappa_1$	$\frac{4}{1+2\alpha_q^+}$	2	$1-\kappa_1$	$\frac{4}{1+2\alpha_q^++2\alpha_q^-}$
$F_q^{p.c.}$	$(1-\kappa_1)\ t_q^\star\left(P^{\text{wall}} + \vec{c}_q \cdot \vec{J}^{\text{wall}}\right)$	$(1-\kappa_1)(\hat{n}_q^- + S_q^-)$			$\alpha^{(u)}\Lambda^-\ \hat{n}_q^-$

Note: When the slippage correction vanishes, the $\alpha_q^\pm$ coefficients take the form of the no-slip schemes previously reported in References 26-28. In the diffusive bounce-back (DBB) kinetic scheme, the $F_q^{p.c.}$ term features a wall pressure P^{wall}; following previous works[21,34,36,40,80,81] we approximate it as $P^{\text{wall}} \approx P(\vec{x}_b)$.

contribution vanishes. Their accuracy with respect to the slip velocity condition, Equation (1), for a microchannel slip flow of arbitrary cross-sectional geometry (planar or curved) will be discussed next.

6.1 | Parabolic schemes

Linkwise schemes pertaining to the class of parabolic schemes operate in a *nonlocal* manner by simultaneously employing populations from the boundary node $\vec{x}_b$ and the nearest fluid node $\vec{x}_b - \vec{c}_q$, that is, using all terms in Equation (40) as given in Table 1. One-point local realizations of linkwise parabolic schemes for the no-slip boundary condition are investigated in a recent studied.[82]

From the implementation standpoint, linkwise parabolic slip schemes can be constructed through the MR framework.[26-28] Different sets of MR coefficients, particularly suited to the slip case, have been derived in previous works;[21,22] here, we focus on the MR1 slip scheme only.

For a given link that is cut by the wall, the closure relation of linkwise parabolic slip schemes is given by:[21,22]

$$
\begin{aligned}
& j_q(\vec{x}_b) + \alpha_q^+\ \partial_q j_q(\vec{x}_b) + \alpha_q^-\ \partial_q^2 j_q(\vec{x}_b) + \mathcal{O}(\epsilon^3) = j_q^{\text{wall}}(\vec{x}_w), \\
& \alpha_q^+ := \left(\delta_q + C\ \lambda_q\right), \quad \alpha_q^- := \left(\frac{\delta_q^2}{2} + C\ \lambda_q\ \delta_q\right), \\
& \lambda_q := \frac{\lambda}{\Theta_q}, \quad \Theta_q := \left(\vec{c}_q \cdot \vec{n}\right), \quad \vec{x}_w = \vec{x}_b + \delta_q\ \vec{c}_q.
\end{aligned} \tag{41}
$$

Note, above $\vec{n}$ denotes the outward unitary normal vector with respect to the wall surface.

Let us evaluate how Equation (41) approximates the tangential component for the slip velocity condition in a microchannel flow of arbitrary geometry. The wall normal component of the flow in the horizontal channel setup is trivially zero, therefore it is disregarded from the analysis. To alleviate notation, let us omit the $\mathcal{O}(\epsilon^3)$ residue in Equation (41). Following the channel flow conditions introduced in Section 2.3, that is, $\vec{j} = j_x(y,z)\ \vec{e}_x$, with the components $\delta_y := \delta_q\ c_{qy}$ and $\delta_z := \delta_q\ c_{qz}$, for the wall cut links $c_{qx}c_{qy} \neq 0$ and $c_{qx}c_{qz} \neq 0$, respectively, the Cartesian reference frame representation of Equation (41) reduces to the equation:

$$
j_x(\vec{x}_b) + \left(\delta_y + C\ \frac{\lambda}{\left(\vec{c}_q \cdot \vec{n}\right)}\ c_{qy}\right)\ \partial_y j_x(\vec{x}_b) + \left(\delta_z + C\ \frac{\lambda}{\left(\vec{c}_q \cdot \vec{n}\right)}\ c_{qz}\right)\ \partial_z j_x(\vec{x}_b)
$$

$$+\left(\frac{\delta_y^2}{2}+C\,\frac{\lambda}{(\vec{c}_q\cdot\vec{n})}\,\delta_y\,c_{qy}\right)\partial_{yy}j_x(\vec{x}_b)+\left(\frac{\delta_z^2}{2}+C\,\frac{\lambda}{(\vec{c}_q\cdot\vec{n})}\,\delta_z\,c_{qz}\right)\partial_{zz}j_x(\vec{x}_b)$$
$$+\left(\delta_y\,\delta_z+C\,\frac{\lambda}{(\vec{c}_q\cdot\vec{n})}\,(\delta_y\,c_{qz}+\delta_z\,c_{qy})\right)\partial_{yz}j_x(\vec{x}_b)=j_x^{\text{wall}}(\vec{x}_w). \tag{42}$$

At this point, and to proceed further, we need to distinguish between the two wall shapes considered in Section 4 and Section 5.

For the *planar wall*, Section 4, whose surface is defined by the outward unitary normal vector $\vec{n}=n_{z'}\,\vec{e}_{z'}$, we employ the coordinate transformation $\vec{e}_y=\cos\theta\,\vec{e}_{y'}-\sin\theta\,\vec{e}_{z'}$ and $\vec{e}_z=\sin\theta\,\vec{e}_{y'}+\cos\theta\,\vec{e}_{z'}$ so that $\delta_y=-\sin\theta\,\delta_{z'}$ and $\delta_z=\cos\theta\,\delta_{z'}$, and $c_{qy}=-\sin\theta\,c_{qz'}$ and $c_{qz}=\cos\theta\,c_{qz'}$, which permits writing the closure relation, Equation (42), as follows:

$$j_x(\vec{x}_b)+(\delta_{z'}+C\,\lambda_{z'})\,\left(-\sin\theta\,\partial_y j_x(\vec{x}_b)+\cos\theta\,\partial_z j_x(\vec{x}_b)\right)$$
$$+\left(\frac{\delta_{z'}^2}{2}+C\,\lambda_{z'}\,\delta_{z'}\right)\left(\sin^2\theta\,\partial_{yy}j_x(\vec{x}_b)+\cos^2\theta\,\partial_{zz}j_x(\vec{x}_b)-\sin 2\theta\,\partial_{yz}j_x(\vec{x}_b)\right)=j_x^{\text{wall}}(\vec{x}_w). \tag{43}$$

For the *curved wall*, Section 5, whose surface is defined by the outward unitary normal vector $\vec{n}=n_r\,\vec{e}_r$, we employ the coordinate transformation $\vec{e}_y=\cos\theta\,\vec{e}_r-\sin\theta\,\vec{e}_\theta$ and $\vec{e}_z=\sin\theta\,\vec{e}_r+\cos\theta\,\vec{e}_\theta$ so that $\delta_y=\cos\theta\,\delta_r$ and $\delta_z=\sin\theta\,\delta_r$, , and $c_{qy}=\cos\theta\,c_{qr}$ and $c_{qz}=\sin\theta\,c_{qr}$, which permits writing the closure relation, Equation (42), as follows:

$$j_x(\vec{x}_b)+\left(\delta_r\left(1-\frac{\delta_r}{2\,r}\right)+C\,\lambda_r\left(1-\frac{\delta_r}{r}\right)\right)\,\left(\cos\theta\,\partial_y j_x(\vec{x}_b)+\sin\theta\,\partial_z j_x(\vec{x}_b)\right)$$
$$+\left(\frac{\delta_r^2}{2}+C\,\lambda_r\,\delta_r\right)\,\left(\partial_{yy}j_x(\vec{x}_b)+\partial_{zz}j_x(\vec{x}_b)\right)=j_x^{\text{wall}}(\vec{x}_w). \tag{44}$$

Above, it was used the identity $\partial_{rr}j_x=-\frac{1}{r^2}\cancel{\partial_{\theta\theta}j_x}-\frac{1}{r}\partial_r j_x+\left(\partial_{yy}j_x+\partial_{zz}j_x\right)=\cos^2\theta\,\partial_{yy}j_x+\sin^2\theta\,\partial_{zz}j_x+\sin 2\theta\,\partial_{yz}j_x$.

In order to compare the closure relations of linkwise and in-node boundary schemes the following subtle detail should be kept in mind. In linkwise boundary schemes[21,22,26-28] the wall normal vector is more conveniently described as pointing outward the fluid domain, that is, $\vec{n}$ points in the same direction of the wall cut links $\vec{c}_q$ so that $\Theta_q>0$. This contrasts with the inward wall normal definition used in the formulation of the LSOB in-node boundary schemes, which fits more naturally their in-node structure. The two approaches can be related by inverting the sign convention between linkwise and in-node LSOB boundary schemes. By doing so, we recognize that Equation (43) matches Equation (15) and Equation (44) matches Equation (30). Such an equivalence demonstrates that, despite the differences between operating principles, the in-node and linkwise approaches reproduce the slip velocity condition as a second-order Taylor series approximation, thus within the same formal order of accuracy.

6.2 | Linear schemes

Linkwise schemes pertaining to the class of linear schemes operate in a *local* manner, by only working with the populations at $\vec{x}_b$, disregarding those at the nearest fluid sites $\vec{x}_b-\vec{c}_q$.

From the implementation standpoint, linkwise linear slip schemes can be constructed by setting $\kappa_{-1}=\overline{\kappa}_{-2}=0$ in Equation (40); the remaining coefficients $\{\kappa_1,\kappa_0,\overline{\kappa}_{-1}\}$ adopt the form given in Table 1 for the three interpolation configurations considered,[21,22,28,83] namely: central linear interpolation (CLI), upwind linear interpolation (MGULI) and downwind linear interpolation (MGDLI). They essentially differ in terms of stability characteristics.[28,83]

For a given link cut by the wall, where the slip velocity boundary condition applies, the closure relation of linkwise linear schemes is expected to be given by:[21,22]

$$j_q(\vec{x}_b) + \alpha_q^+ \; \partial_q j_q(\vec{x}_b) + \text{Error} = j_q^{\text{wall}}(\vec{x}_w) \text{ with Error} = \begin{cases} \mathcal{O}(\epsilon^2) & \text{no} - \text{slip}, \\ \mathcal{O}(\epsilon) & \text{slip}, \end{cases}$$
$$\alpha_q^+ := \left(\delta_q + C\ \lambda_q\right),$$
$$\lambda_q := \frac{\lambda}{\Theta_q}, \quad \Theta_q := \left(\vec{c}_q \cdot \vec{n}\right), \quad \vec{x}_w = \vec{x}_b + \delta_q\ \vec{c}_q. \tag{45}$$

The closure relation, Equation (45), highlights the main drawback of linkwise linear slip schemes: the flow second-order derivative on the boundary is no longer supported by the boundary scheme. This omission has a twofold impact. On the one hand, in the modeling of the no-slip condition, it leads to the well-documented[21,60,83] error scaling with the square of the grid spacing, due to the absence of $\frac{\delta_q^2}{2}\ \partial_q^2 j_q \sim \mathcal{O}(\epsilon^2)$. On the other hand, in the modeling of the slip condition, the lack of this second-order derivative term will imply the absence of the $\left(\frac{\delta_q^2}{2} + C\ \lambda_q\right)\ \partial_q^2 j_q$ term, as denoted in the parabolic closure relation of Equation (41). As the problem physics are governed by $\text{Kn} = \lambda/D_h$, when varying the grid resolution, that is, $D_h \sim N\ \Delta x \sim \frac{1}{\epsilon}$, then λ varies according to the scaling $\lambda = \text{Kn}/\epsilon \sim \mathcal{O}(\epsilon^{-1})$. That is, the intrinsic absence of the curvature term $\partial_q^2 j_q$ in the closure relation of linear slip schemes introduces a first-order error $C\ \lambda_q\ \delta_q\ \partial_q^2 j_q \sim \mathcal{O}(\epsilon)$ in the capturing of the slip velocity condition, degrading their accuracy for the slip problem class. This dual behavior in accuracy is pointed out in Equation (45) by the Error term.

6.3 | Kinetic schemes

Linkwise schemes pertaining to the class of kinetic schemes also operate in a *local* manner, by only using the $\vec{x}_b$ populations. Compared to linear schemes, kinetic schemes are expected to be less accurate since they resort to less information from known populations. Further, they make no use of the wall cut link information δ_q in their operating principle. This implies that the wall boundary node distance should be fixed, which inevitably results in a staircase wall discretization from kinetic schemes.

For the purpose of analysis, we only focus on the DBB scheme, as representative example of kinetic boundary scheme;[21,34,36,40,80,81] the equivalence of this scheme with other kinetic rules has been discussed in a previous study.[21] The DBB update rule nullifies all coefficients in Equation (40), except the κ_1 coefficient and the $F_q^{p.c.}$ correction that enforces the equilibrium state associated to the wall condition, see Table 1.

For a given link cut by the wall, the closure relation of DBB (shared by other kinetic schemes[21]) is expected to be given by:[21,22]

$$j_q(\vec{x}_b) + \text{Error} = j_q^{\text{wall}}(\vec{x}_w), \text{ with Error} = \begin{cases} \mathcal{O}(\epsilon) & \text{no} - \text{slip}, \\ \mathcal{O}(1) & \text{slip}, \end{cases}$$
$$\vec{x}_w = \vec{x}_b + \delta_q\ \vec{c}_q. \tag{46}$$

The closure relation, Equation (46), reveals the unsatisfactory formal accuracy of kinetic schemes. In the no-slip limit, that is, when $\text{Kn} \to 0$, they reduce to the bounce-back (BB) rule where, due to the mid-link boundary location prescribed for each wall cut-link, that is, $\delta_q = \frac{1}{2}\ \forall$ wall cut links, the no-slip condition is unavoidably prescribed on a staircase fashion for nonaligned discretizations. This leads to a downgrade in accuracy, which is revealed by the incomplete closure relation displayed in Equation (46). Here, only the zeroth-order term in the Taylor series approximation is captured, while none of the next order terms are supported, namely the flow slope and curvature are not properly accommodated on nonaligned discretizations. Consequently, the *no-slip* condition prescribed in this case carries the leading order residue $\delta_q\ \partial_q j_q \sim \mathcal{O}(\epsilon)$ in the Taylor series approximation, which explains its first order accuracy, while in the *slip* case, this accuracy further degrades to zeroth-order owing to the leading order residue in the Taylor series approximation becoming $C\ \lambda_q\ \partial_q j_q \sim \mathcal{O}(1)$ due to the coefficient $\lambda = \text{Kn}/\epsilon \sim \mathcal{O}(\epsilon^{-1})$. For a lattice-aligned planar wall with $\delta_q = \frac{1}{2}\ \forall$ wall cut links, the no-slip accuracy of the BB scheme increases its leading-order truncation error to $\mathcal{O}(\epsilon^2)$, and the same also happens to the slip accuracy of the DBB scheme, providing the calibrated coefficient $\kappa_1 = \frac{3\nu - C\lambda}{3\nu + C\lambda}$ shown in Table 1 is employed.[21,34,35] For a detailed list of these and other defects inherent to kinetic schemes we refer to Section IV of a previous work.[21]

6.4 | Corner schemes

Linkwise boundary schemes reproducing the parabolic closure relation, Equation (41), are in general only applicable in a nonlocal manner, that is, they require at least populations from the boundary node $\vec{x}_b$ and the nearest fluid node $\vec{x}_b - \vec{c}_q$. Unfortunately, the discretization of some geometrical elements, such as corners, makes the next linkwise neighbor $\vec{x}_b - \vec{c}_q$ unavailable when prescribing for $\vec{x}_b$. This makes the MR scheme given by full Equation (40) inapplicable.

A viable alternative is the corner scheme proposed in the work,[28] which develops upon the local linkwise strategy with highest accuracy, that is, the *linear schemes* discussed in Section 6.2, and extends it to fulfill the parabolic accuracy, that is, by also capturing the $\left(\frac{\delta_q^2}{2} + C\ \lambda_q\right)\ \partial_q^2 j_q$ term. That is realized by replacing $F_q^{p.c.}$ in Table 1 for the linear schemes by the new correction:

$$F_q^{p.c.}(\vec{x}_b) = (1-\kappa_1)\left(\hat{n}_q^- + S_q^-\right)|_{(\vec{x}_b)} + \alpha^{(u)}\Lambda^-\ \hat{n}_q^-|_{(\vec{x}_b)} + \alpha^{(u)}\ \alpha^-\ \overline{\Delta}_q^2 j_q|_{(\vec{x}_b)}^{F.D.}, \tag{47}$$

with $\alpha^- := \left(\frac{\delta_q^2}{2} + C\ \lambda_q\ \delta_q\right)$ as defined in Equation (41), the momentum source given by $S_q^- = t_q^\star\ \left(\vec{c}_q \cdot \vec{F}\right)$, and the nonlocal momentum Laplacian $\overline{\Delta}_q^2 j_q|^{F.D.}$ approximated as

$$\overline{\Delta}_q^2 j_q|^{F.D.}(\vec{x}_b) = -\frac{1}{\Lambda^+}\left(\hat{n}_q^- + S_q^- - \partial_q^{F.D.} e_q^+\right)|_{(\vec{x}_b)}, \tag{48}$$

with the first-order derivative of the equilibrium term approximated as

$$\partial_q^{F.D.} e_q^+(\vec{x}_b) = -\sum_{\alpha=1}^{d}\left(e_q^+(\vec{x}_b + c_{\bar{q}\alpha}) - e_q^+(\vec{x}_b)\right), \tag{49}$$

where $c_{\bar{q}\alpha}$ denotes the propagation links parallel to the principal coordinate axis. Equation (49) is the main approximation of this strategy and its application should stick with corners only. At other wall geometric features the implicit construction of the second-order derivative term through the nearest fluid node $\vec{x}_b - \vec{c}_q$, that is, the approach followed by MR schemes, see Section 6.1, offers a more robust realization of the parabolic accuracy, which makes it a preferable choice.

7 | NUMERICAL TESTS

The numerical performance of the slip boundary schemes previously introduced is now examined in the simulation of microchannel flows with nontrivial cross-sections, see Figure 3. Here, we compare the numerical accuracy of the proposed in-node LSOB schemes (Lnode and Lwall) against three alternative linkwise implementations, namely: (i) the kinetic (DBB) scheme, a widely used and popular slip scheme; (ii) the CLI slip scheme,[28] an example of a linear accurate

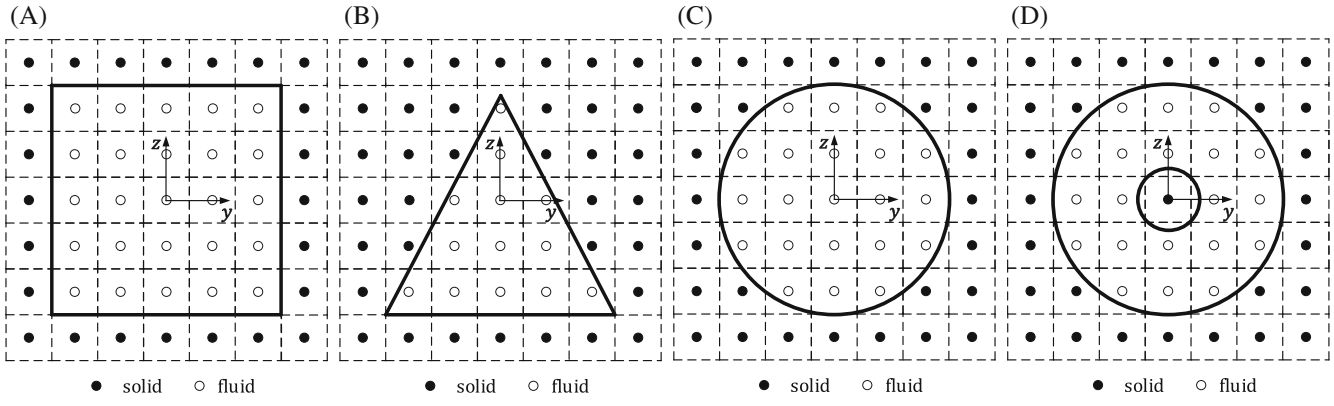

FIGURE 3 Illustration of the microchannel cross-sections considered in this work. In all cases, the Cartesian reference frame (y, z) is centered at the (y_0, z_0) coordinate.

scheme, (iii) the multireflection MR1 slip scheme,[26] an example of a parabolic accurate scheme. The explicit algorithms of these linkwise schemes are summarized in Section 6. The considered schemes represent a trade-off between accuracy and implementation simplicity; in common, they all support viscosity-independent numerical errors. Regarding their implementation, both DBB and CLI slip operate locally on a single-node, while MR1 slip runs on a two-node implementation.[28] In terms of accuracy, taking slip walls nonconforming with the mesh as example, DBB is typically between zeroth- and first-order accuracy, CLI slip is typically first-order accurate, and the MR1 slip is typically second-order accurate; the proof of these error-scales can be found in previous studies.[22] The LSOB slip schemes gather the best of both attributes: they are local and typically second-order accurate.

Numerical accuracy is measured as:

$$\|\mathrm{L}_2(j_x)\| = \frac{\sqrt{\sum \left(j_x^{(\mathrm{num})} - j_x^{(\mathrm{exact})}\right)^2}}{\sqrt{\sum \left(j_x^{(\mathrm{exact})}\right)^2}}, \tag{50}$$

where sums apply to all nonsolid sites. This $\|\mathrm{L}_2(j_x)\|$ measure will be quantified for the five boundary schemes—DBB, CLI slip, MR1 slip, Lnode slip, Lwall slip—applied over the four microchannel cross-sectional shapes: rectangular, triangular, circular and annular; see Figure 3. The application of each boundary scheme is considered for three Kn regimes, namely: hydrodynamic no-slip $\mathrm{Kn} = 0$, moderate slip-flow $\mathrm{Kn} = 0.01$ and large slip-flow $\mathrm{Kn} = 0.1$ regimes.

7.1 | Rectangular duct slip flow

Consider the rectangular duct geometry, shown in Figure 3A, with $\overline{y} = \frac{y-y_0}{W}$ and $\overline{z} = \frac{z-z_0}{H}$, where $-1 \leq (\overline{y}, \overline{z}) \leq 1$, with analytical solution: [18,84,85]

$$j_x^{(\mathrm{exact})}(\overline{y}, \overline{z}) = \frac{2\, F_x\, H^2}{\nu} \sum_{n=1}^{\infty} \frac{\sin \alpha_n \, \cos(\alpha_n\, \overline{z})}{\alpha_n^2\, (\alpha_n + \sin \alpha_n \cos \alpha_n)} \left(1 - \frac{\cosh(\alpha_n\, \zeta\, \overline{y})}{\cosh(\alpha_n\, \zeta) + \frac{4\,\zeta}{1+\zeta}\, C\, \mathrm{Kn}\, \alpha_n \, \sinh(\alpha_n\, \zeta)}\right), \tag{51}$$

where the discrete values of α_n (eigenvalues) are the positive roots of the transcendental equation $\alpha_n \tan \alpha_n = \frac{1+\zeta}{4\,\zeta} \frac{1}{C\ \mathrm{Kn}}$, with $\mathrm{Kn} = \frac{\lambda}{D_h}$ where $D_h = \frac{4(2W+2H)}{4W+4H} = \frac{4\,\zeta}{1+\zeta} H$, and the duct width and height measured as $2W$ and $2H$, respectively, with $\zeta = W/H$ the cross-section aspect ratio; here, it is used $\zeta = 1/2$.

The rectangular cross-section is discretized on a grid-aligned setting. However, walls are shifted $\delta_n = 3/4$ from the boundary nodes, a setting that differs from the traditional halfway $\delta_n = 1/2$ shifting, for example, no-slip[63] and slip[43] works, or the on-grid $\delta_n = 0$ discretization, for example, no-slip[72,77] and slip works.[49,86] This geometry also includes the corners as nontrivial features. These corner sites typically feature links simultaneously cut by two walls where nonlocal boundary schemes, such as the MR1, become inapplicable due to the lack of neighboring nodes to connect to. Here, the MR1 slip scheme is replaced by the local approximation method first proposed in Section 5.2.4 of the original work[28] and extended here, in Section 6.4, to implement the slip condition at corners.

Figure 4 displays the $\|\mathrm{L}_2(j_x)\|$ error as function of Λ, with the grid resolution $N := 2W/\Delta x = 15$ fixed, and the degree of slip varied along three Kn regimes. In contrast with no-slip schemes, where the second-order Λ-effect is the leading-order with linear schemes, in the slip regime the error appears to be dominated by the first-order effects, which explains why the effect of Λ on the accuracy decreases the higher Kn is, that is, the stronger the slip condition becomes.

Figures 5 and 6 display the mesh convergence analysis for $\mathrm{Kn} = 0.01$ and $\mathrm{Kn} = 0.1$, along four different Λ values. The respective convergence rates are listed in Tables 2 and 3. The somewhat insensitivity of the mesh convergence of the slip schemes with Λ is confirmed, which in no-slip simulations tends to happen only in the very fine mesh density limit.[83] The DBB kinetic boundary scheme shows the largest error magnitude and a first-order accuracy. The linear CLI slip scheme diminishes its convergence rate as the slip effect grows, reaching close to first-order at $\mathrm{Kn} = 0.1$. The parabolic slip schemes are the most accurate, revealing Lwall > MR1 > Lnode in terms of $\|\mathrm{L}_2(j_x)\|$ errors. The highest errors and lowest convergence rate of the Lwall slip scheme for large slip-flow effects, that is, at $\mathrm{Kn} = 0.1$, is explained by the weakest enforcement of the slip condition in the boundary populations. The application of Equation (27) on a mesh aligned plane

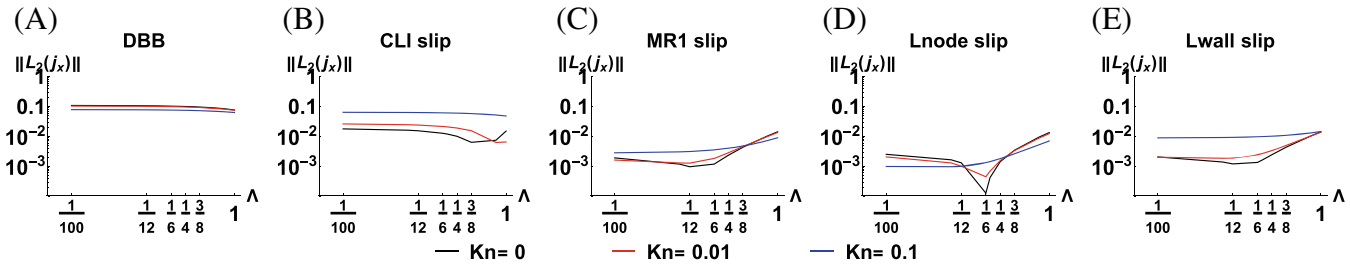

FIGURE 4 Rectangular duct flow. Error estimate $\|L_2(j_x)\|$ versus TRT free relaxation parameter Λ, fixing $N := 2W/\Delta x = 15$, for different LBM slip schemes[Colour figure can be viewed at wileyonlinelibrary.com]

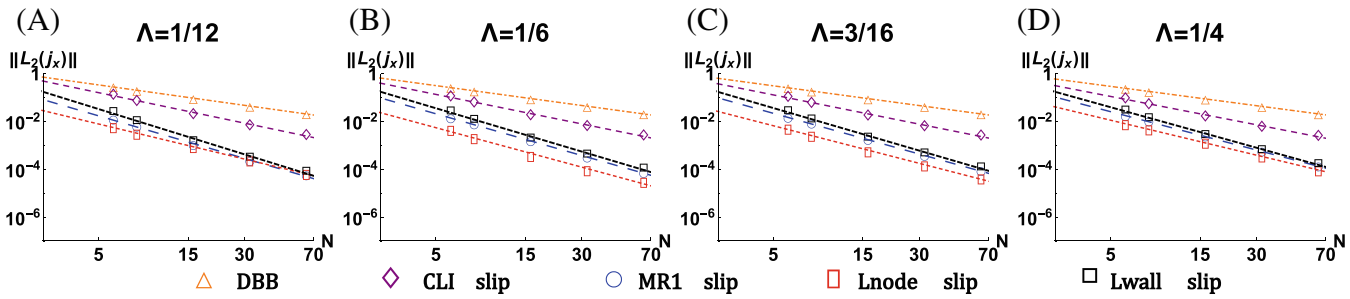

FIGURE 5 Rectangular duct slip flow. Error estimate $\|L_2(j_x)\|$ versus mesh resolution $N := 2W/\Delta x$, fixing $\Lambda = \{1/12,\ 1/6,\ 3/16,\ 1/4\}$. Moderate slip flow regime Kn = 0.01 [Colour figure can be viewed at wileyonlinelibrary.com]

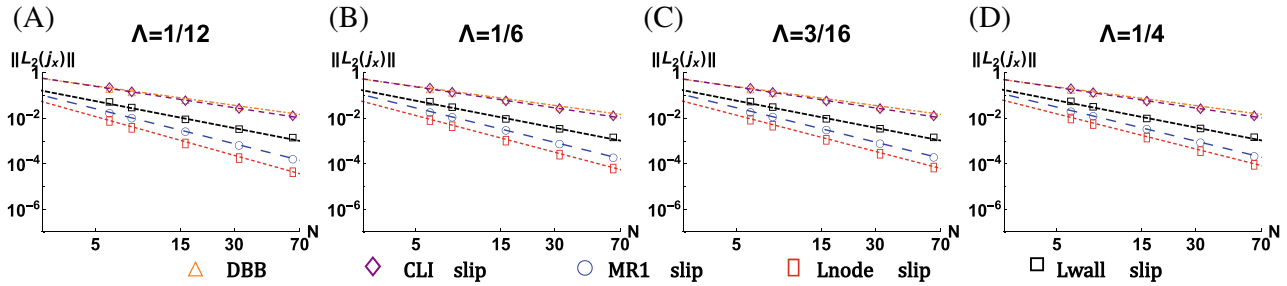

FIGURE 6 Rectangular duct slip flow. Error estimate $\|L_2(j_x)\|$ versus mesh resolution $N := 2W/\Delta x$, fixing $\Lambda = \{1/12,\ 1/6,\ 3/16,\ 1/4\}$. Large slip flow regime Kn = 0.1 [Colour figure can be viewed at wileyonlinelibrary.com]

TABLE 2 Quantification of grid convergence rates in Figure 5, obtained through a least-square linear fitting of the data points

Kn = 0.01	**Λ = 1/12**	**Λ = 1/6**	**Λ = 3/16**	**Λ = 1/4**
DBB	−1.09	−1.07	−1.06	−1.04
CLI slip	−1.63	−1.58	−1.57	−1.52
MR1 slip	−2.28	−2.24	−2.18	−2.06
Lnode slip	−1.88	−2.12	−2.02	−1.87
Lwall slip	−2.43	−2.32	−2.28	−2.17

TABLE 3 Quantification of grid convergence rates in Figure 6, obtained through a least-square linear fitting of the data points

Kn = 0.1	Λ = 1/12	Λ = 1/6	Λ = 3/16	Λ = 1/4
DBB	−1.09	−1.07	−1.06	−1.05
CLI slip	−1.20	−1.18	−1.18	−1.16
MR1 slip	−1.97	−1.94	−1.93	−1.92
Lnode slip	−2.19	−2.07	−2.04	−1.98
Lwall slip	−1.52	−1.53	−1.53	−1.53

wall considers only the slip boundary condition once, for a first-order derivative term, whereas both the Lnode and MR1 slip schemes include the slip condition in all first- and second-order derivative terms.

7.2 | Equilateral triangular duct slip flow

Consider the equilateral triangular duct geometry, shown in Figure 3B, with $\bar{y} = \frac{y-y_0}{L}$ and $\bar{z} = \frac{z-z_0}{L}$, where $-\sqrt{3} \le \bar{y} \le \sqrt{3}$ and $-1 \le \bar{z} \le 2$, with analytical solution:[85,87]

$$j_x^{(\text{exact})}(\bar{y},\bar{z}) = \frac{F_x\, L^2}{12\,\nu}\left(-3\left(\bar{y}^2+\bar{z}^2\right) + \frac{\left(\bar{z}^3 - 3\,\bar{z}\,\bar{y}^2\right)}{(1+C\ \text{Kn})} + 2\frac{\left(2+6\ C\ \text{Kn}+3\ C^2\ \text{Kn}^2\right)}{(1+C\ \text{Kn})}\right) \tag{52}$$

with $2\sqrt{3}\,L$ the length of the equilateral triangular side and $\text{Kn} = \frac{\lambda}{D_h}$ where $D_h = 2\,L$. The triangle discretization is grid-symmetric.

We note that these channel flow solutions result from solving a pure Stokes flow problem, $\nabla^2 j_x = -F_x/\nu$. When represented by the second-order spatial discretization of the LBM-TRT numerical scheme, the leading-order bulk error of such a Stokes problem is given by a fourth-order momentum derivative $\mathcal{E}_{\text{bulk}} \propto \nabla^4 j_x$. Since in this geometry the flow solution is given by a third-order polynomial, Equation (52), then $\mathcal{E}_{\text{bulk}} = 0$. However, the truncation error at boundaries does not vanish similarly since it retains the third-order momentum derivative of Equation (52) as a residue in its Taylor-type approximation.[45] For that reason, this benchmark test is suitable to evaluate the ability of the slip boundary schemes in accommodating slip-flows on non mesh-aligned plane walls. It turns out that, in this test, the boundary accuracy is essentially dominated by the corners forming sharp acute angles rather than the discretization of the inclined planar surfaces.

It is also worth noting that, while the discretization of both rectangular and triangular ducts contains corner populations, only the triangular geometry requires the reconstruction of boundary populations that exactly cross through the corner; in the rectangular duct discretization such corner populations have no projections on the c_{qx} links, hence there are always at equilibrium. For the corners subject to slip, besides the requirement to ensure the continuity of the momentum between the two meeting walls, it is also necessary to preserve the continuity of the momentum derivatives. The fulfillment of this latter condition, within a second-order accuracy level, is not straightforward to realize as it requires the continuity of both first- and second-order derivatives.

Figure 7 displays the $\|\text{L}_2(j_x)\|$ error as function of Λ, with the grid resolution $N = 15/\Delta x$ fixed, and the degree of slip varied along three Kn regimes. The lack of a marked Λ in the minimization of $\|\text{L}_2(j_x)\|$ is mostly explained by the absence of bulk errors. Once again, the insensitivity with Λ becomes more evident the stronger the slip regime is.

Figures 8 and 9 display the mesh convergence analysis for Kn = 0.01 and Kn = 0.1, along four different Λ values. The respective convergence rates are listed in Tables 4 and 5. As expected, the effect of Λ is almost negligible in the behavior of the $\|\text{L}_2(j_x)\|$ curves. The most interesting feature happens in the relation between the convergence rate and the corresponding slip magnitude. It is observed that, when going from a moderate Kn = 0.01 to a large Kn = 0.1 slip-flow regime, all slip schemes tend to loose in the convergence rate between 0.5 and 1 values. This degradation in accuracy makes the DBB kinetic scheme virtually nonconvergent and the parabolic schemes, which for the no-slip problem[47] exhibited an accuracy between second- and third-order, to reduce their convergence rates between 1.7 and 1 at Kn = 0.1. The cause

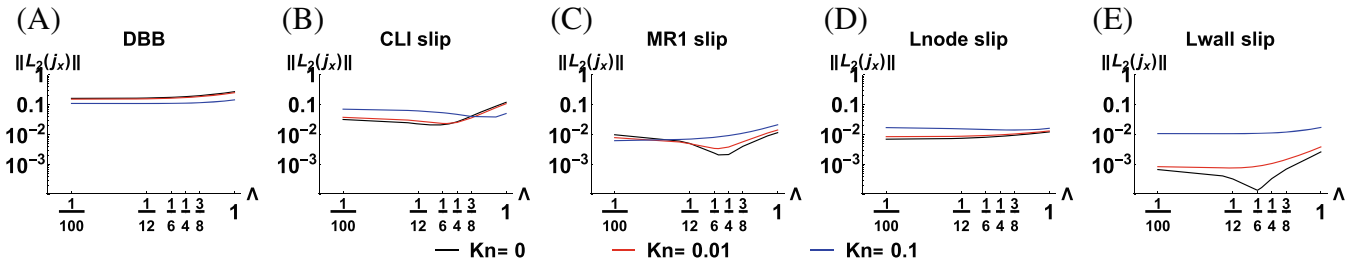

FIGURE 7 Triangular duct flow. Error estimate $\|L_2(j_x)\|$ versus TRT free relaxation parameter Λ, fixing $N := L/\Delta x = 15$, for different LBM slip schemes [Colour figure can be viewed at wileyonlinelibrary.com]

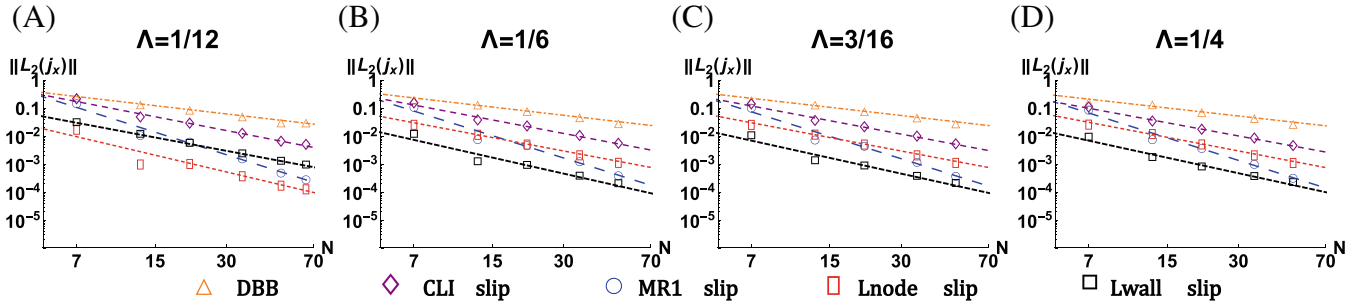

FIGURE 8 Triangular duct slip flow. Error estimate $\|L_2(j_x)\|$ versus mesh resolution $N := L/\Delta x$, fixing $\Lambda = \{1/12,\ 1/6,\ 3/16,\ 1/4\}$. Moderate slip flow regime Kn = 0.01 [Colour figure can be viewed at wileyonlinelibrary.com]

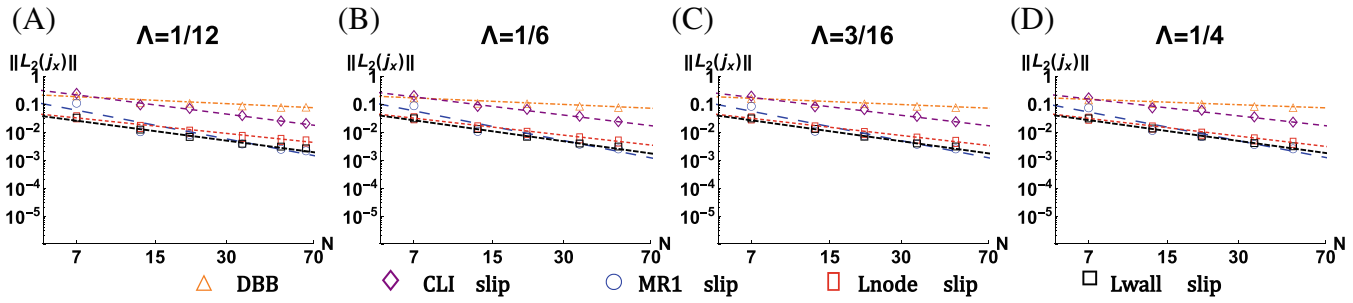

FIGURE 9 Triangular duct slip flow. Error estimate $\|L_2(j_x)\|$ versus mesh resolution $N := L/\Delta x$, fixing $\Lambda = \{1/12,\ 1/6,\ 3/16,\ 1/4\}$. Large slip flow regime Kn = 0.1 [Colour figure can be viewed at wileyonlinelibrary.com]

of this decay lies in the imposition of the slip condition at corners and how the derivatives from each wall at the meeting point are captured. Among the parabolic schemes, the linkwise algorithm, see Section 6.4, appears to handle better the accommodation of the corner momentum derivatives, which is the essential condition for the accurate modeling of the slip condition at corners.

7.3 | Circular pipe slip flow

Consider the circular pipe geometry, shown in Figure 3C, with $\bar{r} = \frac{\sqrt{(y-y_0)^2+(z-z_0)^2}}{R}$, where $0 \leq \bar{r} \leq 1$, with analytical solution:[3,85]

TABLE 4 Quantification of grid convergence rates in Figure 8, obtained through a least-square linear fitting of the data points

Kn = 0.01	Λ = 1/12	Λ = 1/6	Λ = 3/16	Λ = 1/4
DBB	−0.99	−0.98	−0.97	−0.95
CLI slip	−1.64	−1.61	−1.59	−1.56
MR1 slip	−2.68	−2.65	−2.65	−2.68
Lnode slip	−1.99	−1.59	−1.60	−1.62
Lwall slip	−1.59	−1.91	−1.87	−1.84

TABLE 5 Quantification of grid convergence rates in Figure 9, obtained through a least-square linear fitting of the data points

Kn = 0.1	Λ = 1/12	Λ = 1/6	Λ = 3/16	Λ = 1/4
DBB	−0.39	−0.37	−0.35	−0.30
CLI slip	−1.08	−1.03	−1.01	−0.95
MR1 slip	−1.62	−1.68	−1.66	−1.62
Lnode slip	−0.87	−0.96	−0.97	−1.00
Lwall slip	−1.12	−1.18	−1.18	−1.17

$$j_x^{(\text{exact})}(\bar{r}) = \frac{F_x\, R^2}{4\,\nu}\left(1-\bar{r}^2+4\,C\,\text{Kn}\right) \tag{53}$$

with R the pipe radius and $\text{Kn} = \frac{\lambda}{D_h}$ where $D_h = 2\,R$. The circular pipe discretization is grid-symmetric.

The LBM-TRT numerical scheme solves this problem with zero bulk error, $\mathcal{E}_{\text{bulk}} = 0$. So this is the canonical example to benchmark the modeling of curved geometries, since the only source of numerical error comes from the boundary scheme. Surprisingly, this test has been scarcely studied,[43] despite its value in evaluating the performance of LBM slip boundary schemes.

Figure 10 displays the $\|\text{L}_2(j_x)\|$ error as function of Λ, with the grid resolution $N := R/\Delta x = 15$ fixed, and the degree of slip varied along three Kn regimes. As expected, the parabolic schemes reproduce Equation (53) exactly, up to machine precision. The other less accurate slip schemes show a low Λ effect on accuracy, which decreases further with the slip regime magnitude.

Figures 11 and 12 display the mesh convergence analysis for Kn = 0.01 and Kn = 0.1, along four different Λ values. The respective convergence rates are listed in Tables 6 and 7. Once again, parabolic slip schemes prove their exactness for this problem. Conversely, the linear CLI slip scheme decreases its convergence rate to first-order while the DBB kinetic scheme becomes even nonconvergent at Kn = 0.1, which confirms the analysis related to Equations (45) and (46), respectively.

7.4 | Concentric annular pipe slip flow

Consider the concentric annular pipe geometry, shown in Figure 3D, $\bar{r} = \frac{\sqrt{(y-y_0)^2+(z-z_0)^2}}{R_2}$, where $\gamma \le \bar{r} \le 1$, with analytical solution:[18,84,85]

$$j_x^{(\text{exact})}(\bar{r}) = \frac{F_x\, R_2^2}{4\,\nu}\left(1-\bar{r}^2+4\,(1-\gamma)C\,\text{Kn}+\frac{\gamma\,(1-\gamma^2)(1+4\,C\,\text{Kn})}{\gamma\,\log\gamma-2\,(1-\gamma^2)\,C\,\text{Kn}}(2\,(1-\gamma)\,C\,\text{Kn}-\log\bar{r})\right) \tag{54}$$

with R_1 and R_2 the inner and outer pipe radii, $\gamma = R_1/R_2$ the annular gap ratio, here $\gamma = 3/11$, and $\text{Kn} = \frac{\lambda}{D_h}$ where $D_h = 2\,(R_2 - R_1)$. The concentric circular pipes discretization is grid-symmetric.

This problem introduces bulk and boundary errors into the numerical simulation. This makes it a suitable benchmark to study the performance of LBM slip boundary schemes when applied to more challenging setups. Specifically, it permits

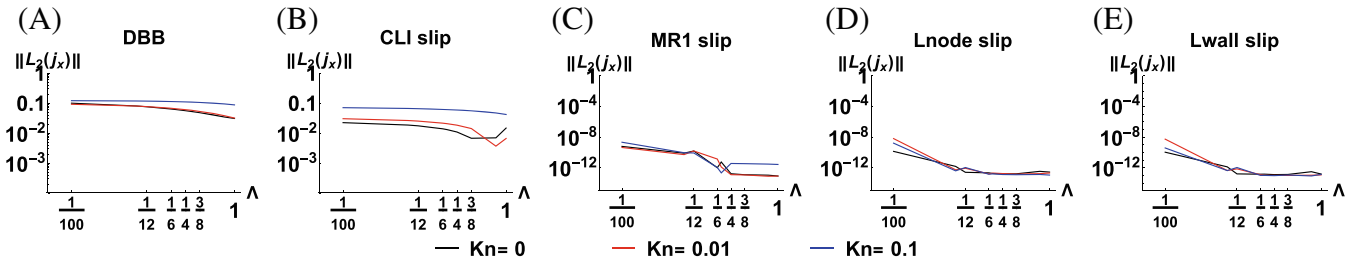

FIGURE 10 Circular pipe flow. Error estimate $\|L_2(j_x)\|$ versus TRT free relaxation parameter Λ, fixing $N := R/\Delta x = 15$, for different LBM slip schemes [Colour figure can be viewed at wileyonlinelibrary.com]

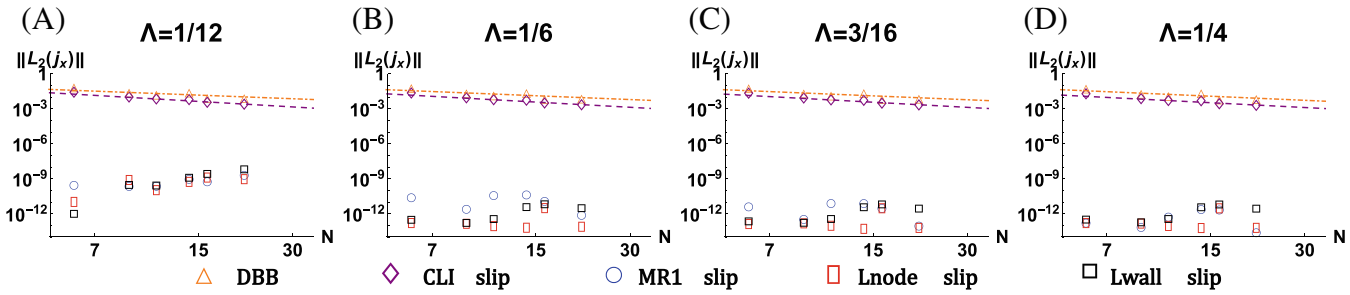

FIGURE 11 Circular pipe flow. Error estimate $\|L_2(j_x)\|$ versus mesh resolution $N := 2R/\Delta x$, fixing $\Lambda = \{1/12,\ 1/6,\ 3/16,\ 1/4\}$. Moderate slip flow regime Kn = 0.01 [Colour figure can be viewed at wileyonlinelibrary.com]

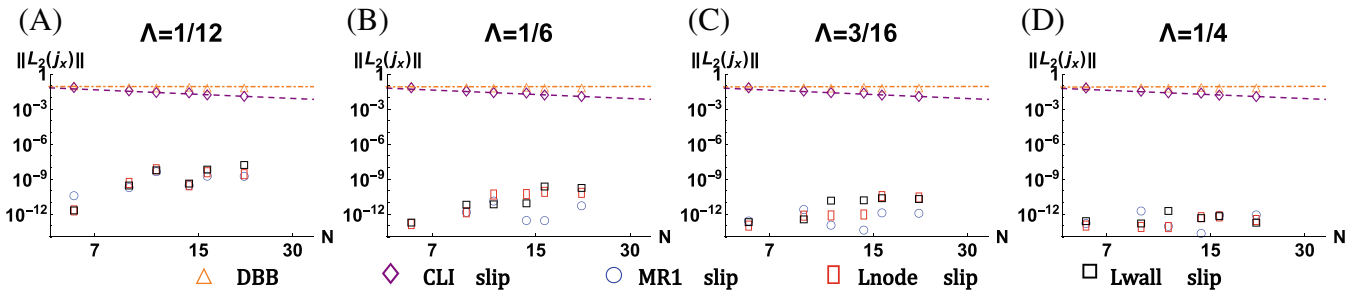

FIGURE 12 Circular pipe flow. Error estimate $\|L_2(j_x)\|$ versus mesh resolution $N := 2R/\Delta x$, fixing $\Lambda = \{1/12,\ 1/6,\ 3/16,\ 1/4\}$. Large slip flow regime Kn = 0.1[Colour figure can be viewed at wileyonlinelibrary.com]

evaluating the accommodation of nonpolynomial solutions on boundaries not conforming with the underlying LBM Cartesian mesh.

Figure 13 displays the $\|L_2(j_x)\|$ error as function of Λ, with the grid resolution $N := (R_2 - R_1)/\Delta x = 15$ fixed, and the degree of slip varied along three Kn regimes. The existence of bulk and boundary errors, as in the rectangular duct studied in Section 7.1, turns the effect of Λ on accuracy more evident. However, with the increase of the wall slip effect, the $\|L_2(j_x)\|$ error tends to become insensitive with Λ. This behavior appears to be universal in the LBM modeling of slip flows, regardless kinetic, linear or parabolic boundary schemes are employed. In conclusion, at large slip regimes, the recommendable procedure to increase the LBM slip-flow accuracy is to refine the mesh whereas the tuning of Λ has a residual impact.

Figures 14 and 15 display the mesh convergence analysis for Kn = 0.01 and Kn = 0.1, along four different Λ values. The respective convergence rates are listed in Tables 8 and 9. The insensitivity of the slip boundary schemes with respect to Λ is again verified in these plots. Referring to the mesh convergence rates, the following trends are observed when going from a moderate Kn = 0.01 to a large Kn = 0.1 slip-flow regime. The kinetic boundary schemes make the solution to decrease from a slightly below first- to a zeroth-order convergence rate, making it nonconvergent at Kn = 0.1. The

TABLE 6 Quantification of grid convergence rates in Figure 11, obtained through a least-square linear fitting of the data points

Kn = 0.01	Λ = 1/12	Λ = 1/6	Λ = 3/16	Λ = 1/4
DBB	−1.03	−1.08	−1.10	−1.17
CLI slip	−1.56	−1.48	−1.46	−1.37

TABLE 7 Quantification of grid convergence rates in Figure 12, obtained through a least-square linear fitting of the data points

Kn = 0.1	Λ = 1/12	Λ = 1/6	Λ = 3/16	Λ = 1/4
DBB	−0.01	0.03	0.04	0.08
CLI slip	−1.17	−1.14	−1.14	−1.12

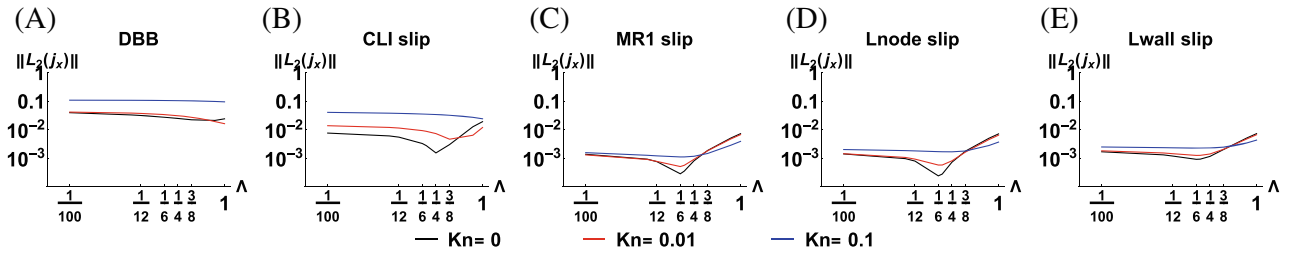

FIGURE 13 Concentric annular pipe flow. Error estimate $\|L_2(j_x)\|$ versus TRT free relaxation parameter Λ, fixing $N := (R_2 - R_1)/\Delta x = 15$, for different LBM slip schemes [Colour figure can be viewed at wileyonlinelibrary.com]

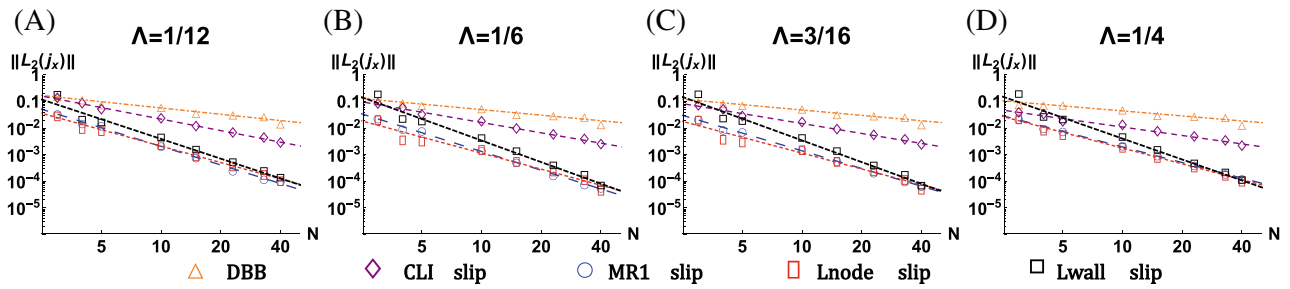

FIGURE 14 Concentric annular pipe flow. Error estimate $\|L_2(j_x)\|$ versus mesh resolution $N := (R_2 - R_1)/\Delta x$, fixing $\Lambda = \{1/12,\ 1/6,\ 3/16,\ 1/4\}$. Moderate slip flow regime Kn = 0.01 [Colour figure can be viewed at wileyonlinelibrary.com]

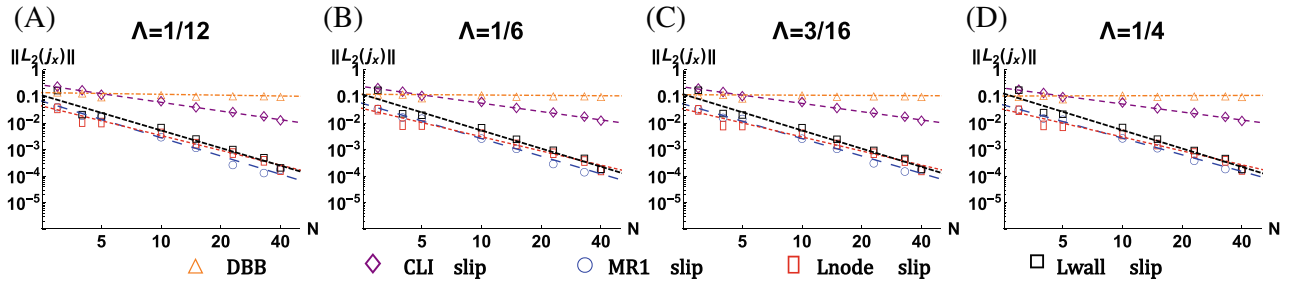

FIGURE 15 Concentric annular pipe flow. Error estimate $\|L_2(j_x)\|$ versus mesh resolution $N := (R_2 - R_1)/\Delta x$ for $\Lambda = \{1/12,\ 1/6,\ 3/16,\ 1/4\}$. Large slip flow regime Kn = 0.1 [Colour figure can be viewed at wileyonlinelibrary.com]

TABLE 8 Quantification of grid convergence rates in Figure 14, obtained through a least-square linear fitting of the data points

Kn = 0.1	Λ = 1/12	Λ = 1/6	Λ = 3/16	Λ = 1/4
DBB	−0.78	−0.69	−0.67	−0.63
CLI slip	−1.44	−1.29	−1.24	−1.05
MR1 slip	−2.32	−2.34	−2.21	−1.94
Lnode slip	−2.05	−2.01	−1.98	−1.97
Lwall slip	−2.47	−2.70	−2.71	−2.61

TABLE 9 Quantification of grid convergence rates in Figure 15, obtained through a least-square linear fitting of the data points

Kn = 0.1	Λ = 1/12	Λ = 1/6	Λ = 3/16	Λ = 1/4
DBB	−0.10	−0.04	−0.03	0.02
CLI slip	−1.09	−1.04	−1.03	−1.00
MR1 slip	−2.29	−2.20	−2.17	−2.08
Lnode slip	−1.85	−1.77	−1.76	−1.73
Lwall slip	−2.20	−2.26	−2.27	−2.30

linear CLI slip scheme holds a first-order convergence rate. The parabolic slip schemes show a second-order convergence rate, with the following accuracy order Lwall > MR1 > Lnode, where both Lwall and MR1 hold their accuracy constantly above second-order.

8 | CONCLUSIONS

This work presents a local and parabolic accurate in-node strategy to implement the slip velocity boundary condition in LBM. The proposed scheme is built upon the recently revived LSOB method for the no-slip walls,[47] which is extended here to include slip effects. The developed scheme is called LSOB slip scheme and, like its no-slip predecessor,[25,45,47] is constructed under two distinct frameworks: the Lnode slip and the Lwall slip, which are devised to operate on node and wall variables, respectively. Both strategies share the same formal order of accuracy, as demonstrated theoretically and also attested by numerical simulations. Specifically, parabolic accurate boundary schemes, such as Lnode, Lwall, and MR1 multireflection,[26,28] all accommodate the parabolic flow solution of the circular pipe geometry, given by Equation (53), in an exact manner (up to the round-off error). Yet, when applied to other flow problems, where the discretization error is inevitable, the LBM solution carries a $\mathcal{O}(\epsilon^2)$ error from bulk and a $\mathcal{O}(\epsilon^3)$ error from boundaries (assuming the use of a parabolic accurate scheme). It is this $\mathcal{O}(\epsilon^3)$ difference in the truncation structure of parabolic boundary schemes, together with how they couple with the bulk solution (via accommodation layers[61,62]), what explains the accuracy differences in the solutions provided by them, despite their similar formal order of accuracy up to $\mathcal{O}(\epsilon^2)$ inclusive.[28,47] The key feature of the parabolic schemes developed here is that they are capable of maintaining the parabolic accuracy with respect to the slip wall condition on planar and curved surfaces, with corners included. We note that slip corners are addressed for the in-node LSOB and also for the previously proposed linkwise slip boundary schemes.[21,22] Although the formulation of in-node and linkwise boundary schemes is presented within the TRT collision model, their extension to other collision operators, such as the multiple-relaxation-time (MRT), is easily manageable,[83] at least for incompressible flows.

Contrary to common practice, this work did not attempt to explore the relationship between the LBM and the kinetic theory to develop a LBM slip boundary scheme. Rather, the prescription of the wall slip condition was explicitly enforced into the LBM boundary populations to guarantee that the intended slip velocity boundary condition is reproduced at the same macroscopic level as the LBM approximates the hydrodynamic equations in bulk. In that regard, the formulation of the LBM boundary scheme searched for the following two main requirements: (i) the fulfillment of the parabolic accuracy with respect to the intended slip boundary condition and (ii) the support of viscosity-independent numerical errors at the boundary, in consistency with the parameterization properties of the TRT model in bulk. These two features, previously reached with the two-node MR slip schemes,[21,22] are accomplished in a local manner by the LSOB slip scheme

proposed here. Although, we recognize that such a compactness is an appealing feature (specially for parallel code implementations), it is fair to mention that it is obtained at the expense of a slightly more evolving formulation (e.g., the LSOB scheme is lattice- and geometry-dependent[47]) compared to the MR slip implementations;[21,22] a general discussion on the pros and cons of the in-node LSOB approach, compared to the more well-established linkwise boundary schemes, is addressed in previous publications on the topic.[25,45,47] Still, within this problem class, the LSOB reconstruction of the boundary populations carries the inherent advantage of explicitly operating with the components of the flow momentum in an independent manner, a feature that naturally fits the slip prescription, whose condition applies along the wall normal direction.

Finally, the work concluded with the examination of the accuracy performance of different families of slip wall implementations (namely, DBB, CLI, MR, and LSOB slip boundary schemes) in the simulation of slow Stokes flow inside 3D microchannels featuring nontrivial cross sectional shapes. Compared to previous studies simulating these geometries with no-slip walls,[47] the modeling of the slip wall condition revealed significantly more challenging. Namely, the necessity to capture both the solution and its derivative at the boundary inherently increased the magnitude of numerical errors, even for schemes formally supporting similar orders of accuracy. In this context, the use of parabolic accurate boundary schemes showed to be critical to preserve the LBM second-order accuracy. Otherwise, the utilization of the more popular kinetic-based or the slightly upgraded linear slip boundary schemes tends to decrease the LBM performance to first- or even zeroth-order accuracy, making LBM an inconsistent numerical scheme for slip-flow problems. A particular delicate point, which will be the subject of a future work, refers to the modeling of the wall slip condition at corners. It appears that even parabolic accurate schemes loose about 0.5 to 1 order accuracy, a loss that grows the larger is the slip regime, which hints to the need for revising the current prescription of the slip boundary condition at sharp corners, either for in-node or linkwise strategies.

ACKNOWLEDGMENTS

This work was supported by FCT, through IDMEC, under LAETA, project UIDB/50022/2020.

DATA AVAILABILITY STATEMENT

The data that support the findings of this study are available from the corresponding author upon reasonable request.

ORCID

Goncalo Silva https://orcid.org/0000-0001-5719-799X
Irina Ginzburg https://orcid.org/0000-0002-2660-350X

REFERENCES

1. Shah RK, London AL. *Laminar Flow Forced Convection in Ducts (Supplement 1 to Advances in Heat Transfer)*. Academic Press; 1978.
2. Sibley DN, Savva N, Kalliadasis S. Slip or not slip? A methodical examination of the interface formation model using two-dimensional droplet spreading on a horizontal planar substrate as a prototype system. *Phys Fluids*. 2012;24:082105. doi:10.1063/1.4742895
3. Zhang W-M, Meng G, Wei X. A review on slip models for gas microflows. *Microfluid Nanofluid*. 2012;13:845-882. doi:10.1007/s10404-012-1012-9
4. Rothstein JP. Slip on superhydrophobic surfaces. *Ann Rev Fluid Mech*. 2010;42:89. doi:10.1146/annurev-fluid-121108-145558
5. Tao S, Guo Z, Wang L-P. Numerical study on the sedimentation of single and multiple slippery particles in a Newtonian fluid. *Powder Technol*. 2017;315:126. doi:10.1016/j.powtec.2017.03.039
6. Drouin G, Fahs M, Droz B, Younes A, Imfeld G, Payraudeau S. Pollutant dissipation at the sediment-water interface: a robust discrete continuum numerical model and recirculating laboratory experiments. *Water Res Res*. 2021;57(30):e2020WR028932. doi:10.1029/2020WR028932
7. Yoshimura A, Prudhomme RK. Wall slip corrections for couette and parallel flow viscometers. *J Rheol*. 1988;32:53-67. doi:10.1122/1.549963
8. Jansons KM. Determination of the macroscopic (partial) slip boundary condition for a viscous flow over a randomly rough surface with a perfect slip microscopic boundary condition. *Phys Fluids*. 1988;31:15. doi:10.1063/1.866563
9. Vinogradova OI, Yakubov GE. Surface roughness and hydrodynamic boundary conditions. *Phys Rev E*. 2006;73:045302. doi:10.1103/PhysRevE.73.045302
10. Choi CH, Westin KJA, Breuer KS. Apparent slip flows in hydrophilic and hydrophobic microchannels. *Phys Fluids*. 2003;15:2897. doi:10.1063/1.1605425
11. Sharipov F, Seleznev V. Data on internal rarefied gas flows. *J Phys Chem Ref Data*. 1998;27:657-706. doi:10.1063/1.556019
12. Agrawal A, Prabhu SV. Deduction of slip coefficient in slip and transition regimes from existing cylindrical Couette flow data. *Exp Therm Fluid Sci*. 2008;32:991-996. j.expthermflusci.2007.11.010.

13. Silva G, Leal N, Semiao V. Determination of microchannels geometric parameters using micro-PIV. *Chem Eng Res Des*. 2009;87:298-306. j.cherd.2008.08.009.
14. Ferrás LL, Nóbrega JM, Pinho FT. Implementation of slip boundary conditions in the finite volume method: new techniques. *Int J Numer Meth Fluids*. 2013;72:724. doi:10.1002/fld.3765
15. Chourushi T, Rahimi A, Singh S, Myong RS. Computational simulations of near continuum gas flow using Navier-Stokes-Fourier equations with slip and jump conditions based on the modal discontinuous Galerkin method. *Adv Aerodyn*. 2020;2:8. doi:10.1186/s42774-020-00032-z
16. Sone Y. *Kinetic Theory and Fluid Dynamics*. Birkhäuser; 2002.
17. Karniadakis G, Beskok A, Aluru N. *Microflows and Nanoflows*. Springer; 2005.
18. Duan Z, Muzychka YS. Slip flow in non-circular microchannels. *Microfluid Nanofluid*. 2007;3:473-484. doi:10.1007/s10404-006-0141-4
19. Navier CLM. Sur les lois du Mouvement des Fluides. *Mem Acad Roy Sci Inst Fr*. 1827;6:389-440. doi:10.1063/1.556019
20. Maxwell JC. On stresses in rarified gases arising from inequalities of temperature. *Philos Trans R Soc Lond*. 1879;170:231.
21. Silva G, Semiao V. Consistent lattice Boltzmann modeling of low-speed isothermal flows at finite Knudsen numbers in slip-flow regime: Application to plane boundaries. *Phys Rev E*. 2017;96:013311. doi:10.1103/PhysRevE.96.013311
22. Silva G. Consistent lattice Boltzmann modeling of low-speed isothermal flows at finite Knudsen numbers in slip-flow regime. II. Application to curved boundaries. *Phys Rev E*. 2018;98:023302. doi:10.1103/PhysRevE.98.023302
23. Dione I, Tibirna C, Urquiza J. Stokes equations with penalised slip boundary conditions. *Int J Comput Fluid Dyn*. 2013;27:283. doi:10.1080/10618562.2013.821114
24. Westerkamp A, Torrilhon M. Curvature-induced instability of a Stokes-like problem with non-standard boundary conditions. *Appl Numer Math*. 2017;121:96-114. doi:10.1016/j.apnum.2017.06.012
25. Ginzburg I, d'Humières D. Local second-order boundary method for lattice Botlzmann models. *J Stat Phys*. 1996;64:927-971. doi:10.1007/BF02174124
26. Ginzburg I, d'Humières D. Multi-reflection boundary conditions for lattice Botlzmann models. *Phys Rev E*. 2003;68:066614. doi:10.1103/PhysRevE.68.066614
27. Ginzburg I. Generic boundary conditions for Lattice Boltzmann models and their application to advection and anisotropic-dispersion equations. *Adv Wat Res*. 2005;28:1196-1216. doi:10.1016/j.advwatres.2005.03.009
28. Ginzburg I, Verhaeghe F, d'Humières D. Two-relaxation-time lattice Boltzman scheme: about parametrization, velocity, pressure and mixed conditions. *Commun Comp Phys*. 2008;3:427.
29. Chen S, Doolen G. Lattice Boltzmann method for fluid flows. *Ann Rev Fluid Mech*. 1998;30:329. doi:10.1146/annurev.fluid.30.1.329
30. Aidun CK, Clausen JR. Lattice-Boltzmann method for complex flows. *Annu Rev Fluid Mech*. 2010;42:439. doi:10.1146/annurev-fluid-121108-145519
31. Krüger T, Kusumaatmaja H, Kuzmin A, Shardt O, Silva G, Viggen EM. *The Lattice Boltzmann Method - Principles and Practice*. 1st ed. Springer; 2016.
32. Succi S. *The Lattice Boltzmann Equation: For Complex States of Flowing Matter*. Oxford University Press; 2018.
33. Ansumali S, Karlin IV. Kinetic boundary conditions in the lattice Boltzmann method. *Phys Rev E*. 2002;66:026311. doi:10.1103/PhysRevE.66.026311
34. Guo Z, Shi B, Zhao TS, Zheng C. Discrete effects on boundary conditions for the lattice Boltzmann equation in simulating microscale gas flows. *Phys Rev E*. 2007;76:056704. doi:10.1103/PhysRevE.76.056704
35. Guo Z, Zheng C. Analysis of lattice Boltzmann equation for microscale gas flows: Relaxation time, Boundary condition, and Knudsen layer. *Int J Comput Fluid Dyn*. 2008;22:465. doi:10.1080/10618560802253100
36. Verhaeghe F, Luo L-S, Blanpain B. Lattice Boltzmann modeling of microchannel flow in slip flow regime. *J Comput Phys*. 2009;228:147. doi:10.1016/j.jcp.2008.09.004
37. Reis T, Dellar PJ. Lattice Boltzmann simulations of pressure-driven flows in microchannels using Navier–Maxwell slip boundary conditions. *Phys Fluids*. 2012;24:112001. doi:10.1063/1.4764514
38. Yang L, Yu Y, Hou G, Wang K, Xiong Y. Boundary conditions with adjustable slip length for the lattice Boltzmann simulation of liquid flow. *Comput Fluids*. 2018;174:200-212. doi:10.1016/j.compfluid.2018.08.002
39. Mohammed S, Reis T. Lattice Boltzmann method with moment-based boundary conditions for rarefied flow in the slip regime. *Phys Rev E*. 2021;104:045309. doi:10.1103/PhysRevE.104.045309
40. Tao S, Guo Z. Boundary condition for lattice Boltzmann modeling of microscale gas flows with curved walls in the slip regime. *Phys Rev E*. 2015;91:043305. doi:10.1103/PhysRevE.91.043305
41. Wang L, Yin X. Apparent permeability of flow through periodic arrays of sphereswith first-order slip. *Powder Technol*. 2017;311:313. doi:10.1016/j.powtec.2017.01.072
42. Seta T, Hayashi K, Tomiyama A. Analytical and numerical studies of the boundary slip in the immersed boundary-thermal lattice Boltzmann method. *Int J Numer Meth Fluids*. 2020;86:454. doi:10.1002/fld.4462
43. Aminpour M, Galindo-Torres SA, Scheuermann A, Li L. Slip-flow lattice-Boltzmann simulations in ducts and porous media: A full rehabilitation of spurious velocities. *Phys Rev E*. 2018;98:043110. doi:10.1103/PhysRevE.98.043110
44. Wang L, Tao S, Hu J, Zhang K, Lu G. Curved boundary conditions of the lattice Boltzmann method for simulating microgaseous flows in the slip flow regime. *Comput Fluids*. 2021;230:105117. doi:10.1016/j.compfluid.2021.105117
45. Ginzburg I, d'Humières D. Local second-order boundary method for lattice Botlzmann models. Part II. Application to Poisson equation in complicated geometries. Unpublished; 1995.

46. Ginzburg I, Steiner C. Lattice Boltzmann model for free-surface flow and its application to filling process in casting. *J Comput Phys*. 2003;185:61-99. doi:10.1016/S0021-9991(02)00048-7
47. Silva G, Ginzburg I. Reviving the local second-order boundary approach within the two-relaxation-time lattice Boltzmann modelling. *Phil Trans R Soc A*. 2020;378:20190404. doi:10.1098/rsta.2019.0404
48. d'Humières D, Ginzburg I. Viscosity independent numerical errors for Lattice Boltzmann models: From recurrence equations to "magic" collision numbers. *Comput Math Appl*. 2009;58:823. doi:10.1016/j.camwa.2009.02.008
49. Sinnah ZB. *Lattice Boltzmann Method For 2D and 3D Flows in Channels and Ducts with Slip and no-Slip Walls*. PhD thesis. University of Plymouth; 2020. http://hdl.handle.net/10026.1/16136
50. Ginzburg I. Consistent lattice Boltzmann schemes for the Brinkman model of porous flow and infinite Chapman-Enskog expansion. *Phys Rev E*. 2008;77:066704. doi:10.1103/PhysRevE.77.066704
51. Ginzburg I. Truncation errors, exact and heuristic stability analysis of two-relaxation-times lattice Boltzmann schemes for anisotropic advection–Diffusion equation. *Commun Comput Phys*. 2012;11(5):1439-1502. doi:10.4208/cicp.211210.280611a
52. Chapman S, Cowling T. *The Mathematical Theory of Non-Uniform Gases*. Cambridge University Press; 1970.
53. Ginzburg I. Steady-state two-relaxation-time lattice Boltzmann formulation for transport and flow, closed with the compact multi-reflection boundary and interface-conjugate schemes. *J Comp Sci*. 2021;54:101215. doi:10.1016/j.jocs.2020.101215
54. Mavriplis D. Multigrid solution of the steady-state lattice Boltzmann equation. *Comput Fluids*. 2006;35:793. doi:10.1016/j.compfluid.2005.07.020
55. Zhang L, Zeng Z, Xie H, et al. An alternative second order scheme for curved boundary condition in lattice Boltzmann method. *Comput Fluids*. 2015;144:193-202. doi:10.1016/j.compfluid.2015.03.006
56. Bauer M, Silva G, Rüde U. Truncation errors of the D3Q19 lattice model for the lattice Boltzmann method. *J Comput Phys*. 2020;405:109111. doi:10.1016/j.jcp.2019.109111
57. Ginzburg I, Silva G, Talon L. Analysis and improvement of Brinkman lattice Boltzmann schemes: Bulk, boundary, interface. Similarity and distinctness with finite elements in heterogeneous porous media. *Phys Rev E*. 2015;91:023307. doi:10.1103/PhysRevE.91.023307
58. Silva G, Talon L, Ginzburg I. Low-and high-order accurate boundary conditions: From Stokes to Darcy porous flow modeled with standard and improved Brinkman lattice Boltzmann schemes. *J Comput Phys*. 2017;335:50. doi:10.1016/j.jcp.2017.01.023
59. Cornubert R, d'Humières D, Levermore D. A Knudsen layer theory for lattice gases. *Phys D*. 1991;47:241-259. doi:10.1016/0167-2789(91)90295-K
60. Ginzburg I, Verhaeghe F, d'Humières D. Study of simple hydrodynamic solutions with the two-relaxation- times Lattice Boltzmann scheme. *Commun Comput Phys*. 2008;3:519.
61. Ginzburg I, Roux L, Silva G. Local boundary reflections in lattice Boltzmann schemes: Spurious boundary layers and their impact on the velocity, diffusion and dispersion. *C R Mec*. 2015;343:518-532. doi:10.1016/j.crme.2015.03.004
62. Ginzburg I. Spurious interface and boundary behaviour beyond of physical solution in the Lattice Boltzmann schemes. *J Comp Phys*, 2021;431:109986. doi:10.1016/j.jcp.2020.109986
63. Zou Q, He X. On pressure and velocity boundary conditions for the lattice Boltzmann BGK model. *Phys Fluids*. 1997;9:1592-1598. doi:10.1063/1.869307
64. Ginzburg I. *Boundary Conditions Problems in Lattice Gas Methods for Single and Multiple Phases*. Ph.D. thesis. University Paris VI; 1994.
65. Skordos PA. Initial and boundary conditions for the lattice Boltzmann method. *Phys Rev E*. 1993;48:4823. doi:10.1103/PhysRevE.48.4823
66. Halliday I, Hammond LA, Care CM. Enhanced closure scheme for lattice Boltzmann equation hydrodynamics. *J Phys A Math Gen*. 2002;35:157-166. doi:10.1088/0305-4470/35/12/102
67. Hollis AP, Halliday I, Care CM. An accurate and versatile lattice closure scheme for lattice Boltzmann equation fluids under external forces. *J Comput Phys*. 2008;227:8065-8082. doi:10.1016/j.jcp.2008.05.007
68. Dorschner B, Chikatamarla SS, Bösch F, Karlin IV. Grad's approximation for moving and stationary walls in entropic lattice Boltzmann simulations. *J Comput Phys*. 2015;295:340-354. doi:10.1016/j.jcp.2015.04.017
69. Verschaeve JCG, Müller B. A curved no-slip boundary condition for the lattice Boltzmann method. *J Comput Phys*. 2010;229:6781-6803. doi:10.1016/j.jcp.2010.05.022
70. Mohammadipour OR, Niazmand H, Mirbozorgi SA. Alternative curved-boundary treatment for the lattice Boltzmann method and its application in simulation of flow and potential fields. *Phys Rev E*. 2014;89:013309. doi:10.1103/PhysRevE.89.013309
71. Junk M, Yang Z. One-point boundary condition for the lattice Boltzmann method. *Phys Rev E*. 2005;72:066701. doi:10.1103/PhysRevE.72.066701
72. Latt J, Chopard B, Malaspinas O, Deville M, Michler A. Straight velocity boundaries in the lattice Boltzmann method. *Phys Rev E*. 2008;77:056703. doi:10.1103/PhysRevE.77.056703
73. Malaspinas O, Chopard B, Latt J. General regularized boundary condition for multi-speed lattice Boltzmann models. *Comput Fluids*. 2011;49:29-35. doi:10.1016/j.compfluid.2011.04.010
74. Verschaeve JCG. Involving the Navier–Stokes equations in the derivation of boundary conditions for the lattice Boltzmann method. *Phil Trans R Soc A*. 2011;369:2184-2192. doi:10.1098/rsta.2011.0045
75. Noble NR, Chen S, Georgiadis JG, Buckius RO. A consistent hydrodynamic boundary condition for the lattice Boltzmann method. *Phys Fluids*. 1995;7:203-209. doi:10.1063/1.868767
76. Bennett S, Asinari P, Dellar PJ. A lattice Boltzmann model for diffusion of binary gas mixtures that includes diffusion slip. *Int J Numer Methods Fluids*. 2012;69:171. doi:10.1002/fld.2549

77. Krastins I, Kao A, Pericleous K, Reis T. Moment-based boundary conditions for straight on-grid boundaries in three-dimensional lattice Boltzmann simulations. *Int J Numer Meth Fluids*. 2020;92:1948. doi:10.1002/fld.4856
78. Verschaeve JCG. Analysis of the lattice Boltzmann Bhatnagar-Gross-Krook no-slip boundary condition: Ways to improve accuracy and stability. *Phys Rev E*. 2009;80:036703. doi:10.1103/PhysRevE.80.036703
79. Reis T. On the lattice Boltzmann deviatoric stress: analysis, boundary conditions, and optimal relaxation times. *SIAM J Sci Comput*. 2020;42:B397-B424. doi:10.1137/19M1244846
80. Guo Z, Shi B, Zheng C. Velocity inversion of micro cylindrical Couette flow: A lattice Boltzmann study. *Comput Math Appl*. 2011;61:3519-3527. doi:10.1016/j.camwa.2010.01.022
81. Prasianakis N, Ansumali S. Microflow simulations via the lattice Boltzmann method. *Commun Comput Phys*. 2011;9:1128-1136. doi:10.4208/cicp.301009.271010s
82. Ginzburg I, Silva G, Marson F, Chopard B, Latt J. Unified directional parabolic-accurate Lattice Boltzmann boundary schemes for grid-rotated narrow gaps and curved walls in creeping and inertial fluid flows. *Phys Rev E*. (in preparation).
83. Khirevich S, Ginzburg I, Tallareka U. Coarse-and fine-grid numerical behavior of MRT/TRT lattice-Boltzmann schemes in regular and random sphere packings. *J Comput Phys*. 2015;281:708-742. doi:10.1016/j.jcp.2014.10.038
84. Ebert WA, Sparrow EM. Slip flow in rectangular and annular ducts. *J Basic Eng*. 1965;87:1018-1024. doi:10.1115/1.3650793
85. Wang CY. Brief review of exact solutions for slip-flow in ducts and channels. *J Fluids Eng*. 2012;134:094501. doi:10.1115/1.4007232
86. Ahmed NK, Harting M. A boundary condition with adjustable slip length for lattice Boltzmann simulations. *J Stat Mech Theory Exp*. 2009;2009:P09017. doi:10.1088/1742-5468/2009/09/P09017
87. Wang CY. Slip flow in a triangular duct—An exact solution. *Z Angew Math Mech*. 2003;83:629-631. doi:10.1002/zamm.200310057

How to cite this article: Silva G, Ginzburg I. Slip velocity boundary conditions for the lattice Boltzmann modeling of microchannel flows. *Int J Numer Meth Fluids*. 2022;94(12):2104-2136. doi: 10.1002/fld.5138